Bigger Isn't Always Memorizing: Early Stopping Overparameterized Diffusion Models

Anonymous authors
Paper under double-blind review

Abstract

Diffusion probabilistic models have become a cornerstone of modern generative AI, yet the mechanisms underlying their generalization remain poorly understood. In fact, if these models were perfectly minimizing their training loss, they would just generate data belonging to their training set, i.e., memorize, as empirically found in the overparameterized regime. We revisit this view by showing that, in highly overparameterized diffusion models, generalization in natural data domains is progressively achieved during training *before* the onset of memorization. Our results, ranging from image to language diffusion models, systematically support the empirical law that memorization time is proportional to the dataset size, consistent with a kernel-regression spectral argument for fitting the empirical score at low noise. Generalization vs. memorization is then best understood as a competition between time scales. We show that this phenomenology is recovered in diffusion models learning a simple probabilistic context-free grammar with random rules, where generalization corresponds to the hierarchical acquisition of deeper grammar rules as training time grows, and the generalization cost of early stopping can be characterized. We summarize these results in a phase diagram. Overall, our results support that a principled early-stopping criterion – scaling with dataset size – can effectively optimize generalization while avoiding memorization, with direct implications for hyperparameter transfer and privacy-sensitive applications.

1 Introduction

Diffusion models (Sohl-Dickstein et al., 2015; Ho et al., 2020) have recently emerged as a transformative paradigm in generative AI, enabling the synthesis of high-quality data across a wide range of modalities – images (Dhariwal & Nichol, 2021; Rombach et al., 2022; Ramesh et al., 2022), videos (Ho et al., 2022; Blattmann et al., 2023), text (Austin et al., 2021; Sahoo et al., 2024; Shi et al., 2024; Nie et al., 2025), and complex 3D structures such as molecular conformations and protein sequences (Watson et al., 2023; Alakhdar et al., 2024). Their strength lies in their scalability in generating diverse, high-fidelity samples by reversing a progressive noise addition process, making them both versatile and robust across domains. At the heart of this process is the estimation of a *score function* (Song & Ermon, 2019; Song et al., 2020): a noise-dependent vector field that guides denoising by pointing in the direction of increasing data likelihood. Since this function is learned from the empirical training distribution, minimizing the training loss optimally leads the model to reproduce the training data itself – a phenomenon known as *memorization* (Carlini et al., 2023; Somepalli et al., 2022). This phenomenon is observed in practical settings and raises significant privacy and copyright concerns, as models trained on sensitive or proprietary data may inadvertently regenerate such content, exposing private information or violating intellectual property rights (Wu et al., 2022; Matsumoto et al., 2023; Hu & Pang, 2023). In contrast, *generalization* corresponds to the model producing novel samples that are consistent with, but not identical to, the training data, thereby approximating the broader target distribution.

Despite the empirical success of diffusion models, the mechanisms underlying their ability to generalize remain poorly understood. A prevailing view – rooted in classical learning theory – is that generalization depends on *underparameterization* (Yoon et al., 2023; Zhang et al., 2023; Kadkhodaie et al., 2023): only models that lack the capacity to memorize their training data are expected to generalize. In this work, we go beyond this view by demonstrating that even heavily overparameterized diffusion models exhibit generalization during

training *before* they start memorizing the training data. We systematically investigate this phenomenon, showing that generalization and memorization are not mutually exclusive but unfold as distinct temporal phases of training. Our main contributions are as follows:

- We empirically demonstrate the transition from generalization to memorization during training in a range of overparametrized diffusion models – including Improved DDPM (Nichol & Dhariwal, 2021), Stable Diffusion (Rombach et al., 2022), MD4 (Shi et al., 2024), and D3PM (Austin et al., 2021) – on both images and text data. We measure memorization and generalization metrics and systematically vary the training set size, showing that generalization improves gradually, before the onset of memorization.
- In all settings, we observe the empirical law that the onset of memorization requires a number of training steps proportional to the training set size. We provide a theoretical argument in a simplified kernel regime: at fixed low diffusion noise, this spectral argument identifies a timescale for fitting the empirical score that scales linearly with the training set size. We confirm this prediction numerically with one-hidden-layer networks in the NTK regime. This result is consistent with and generalizes the contemporaneous result of Bonnaire et al. (2025) for high-dimensional random features.
- We study a discrete diffusion model trained to learn a simple *probabilistic context-free grammar*, where the number of training steps or samples required to generalize is known to be polynomial in the sequence length (Favero et al., 2025). We show that for moderate training set sizes, the diffusion model only learns the lowest levels of the hierarchical grammar rules – corresponding to partial generalization – before starting to memorize. For larger training set sizes, the onset of memorization appears after perfect total generalization is achieved. These results lead to a phase diagram for memorization and generalization as a function of sample complexity and training time.

On the theoretical level, these findings call for a revision of the view of generalization in diffusion models as being solely determined by model capacity, showing that generalization arises *dynamically during training* in overparameterized diffusion models. On the practical level, our results suggest that early stopping and dataset-size-aware training protocols may be optimal strategies for preserving generalization and avoiding memorization as the size of diffusion models is scaled up. In fact, these results provide a principled handle on the verbatim regeneration of training data, with direct implications for privacy and for mitigating training-data extraction in generative AI, in contrast to heuristic procedures that lack quantitative grounding (Dockhorn et al., 2022; Vyas et al., 2023; Chen et al., 2024).

2 Diffusion Models and the Score Function

Denoising diffusion models are generative models that sample from a data distribution $q(x_0)$ by reversing a noise addition process (Sohl-Dickstein et al., 2015; Ho et al., 2020; Song & Ermon, 2019; Song et al., 2020). The *forward process* generates a sequence of increasingly noised data $\{x_t\}_{1\leq t\leq T}$, with distribution $q(x_1,\ldots,x_T|x_0)=\prod_{t=1}^{T} q(x_t|x_{t-1})$, where t indicate the time step in a sequence $[0,\ldots,T]$. At the final time T, x_T is distributed as pure noise. The *backward process* reverts the forward one by gradually removing noise and is obtained by learning the backward transition kernels $p_\theta(x_{t-1}|x_t)$ using a neural network with parameters θ.

In practice, the key quantity the model must learn is the *denoiser*, i.e., the posterior expectation $\mathbb{E}_{q(x_0|x_t)}[x_0]$, which encodes all the information needed to reverse the forward process at each noise level. Training is performed by minimizing a variational bound on the negative log-likelihood of the data (Sohl-Dickstein et al., 2015; Ho et al., 2020), whose precise form depends on the forward process (see below). We generically refer to the noise-level-dependent function learned by the model as the *score function*, following standard usage in the continuous case; in the discrete case, this should be understood as the learned denoiser.

Since the variational bound involves an expectation over the data distribution $q(x_0)$, in practice it is estimated from P training examples $\{x_0^{(i)}\}_{i\in[P]}$, drawn from the empirical distribution $\hat{q}(x_0)=P^{-1}\sum_{i=1}^{P}\delta(x_0-x_0^{(i)})$. Perfectly minimizing this empirical loss amounts to learning the *empirical score*, which generates $\hat{q}(x_0)$: as a result, diffusion models would only generate data of the training set, corresponding to *memorization*. Their generalization abilities, therefore, derive from not perfectly minimizing the empirical loss.

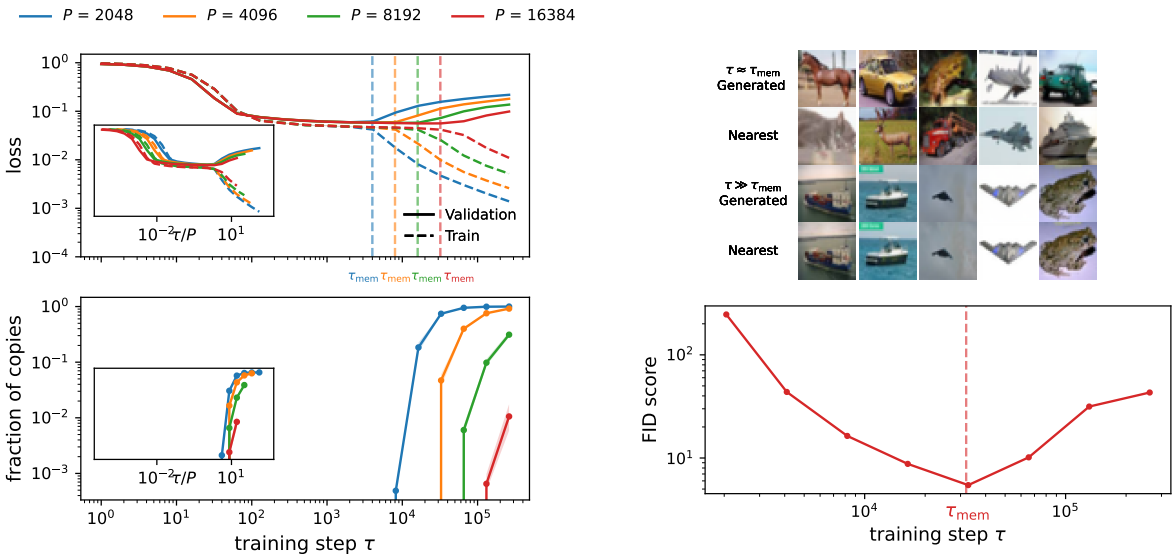

Figure 1: **Memorization dynamics in vision diffusion models.** *Left:* Train loss, validation loss, and fraction of copied images as a function of training steps τ for iDDPM models trained on CIFAR-10 with varying training set sizes P. Both losses decrease initially, indicating generalization, but diverge at the onset of memorization (τ_{mem}, vertical dashed lines), where the models start copying training data. Larger training sets delay τ_{mem}, scaling approximately linearly with P (insets, in which curves are plotted against τ/P). Lines: mean across 3 independent runs; shaded bands: ± 1 std. *Right, top:* Samples generated by the model trained on $P = 16{,}384$ images at early stopping ($\tau \approx \tau_{\text{mem}}$) and well past memorization ($\tau \gg \tau_{\text{mem}}$), each shown above their nearest neighbor in the training set: at τ_{mem} the generations are novel, while at long training they reproduce training examples. *Right, bottom:* FID against the union of CIFAR-10 train and test splits as a function of τ for the same model; the FID is non-monotonic, with a minimum at $\tau \approx \tau_{\text{mem}}$.

Diffusion processes For continuous data, like images, the forward process corresponds to time-discretized Gaussian diffusion with $q(x_t|x_{t-1}) = \mathcal{N}(x_t; \sqrt{1-\beta_t}x_{t-1}, \beta_t \mathbb{I})$, where $\mathcal{N}$ represents the normal distribution and the sequence $\{\beta_t\}_{1 \leq t \leq T}$ is the variance schedule. In this case, the denoiser is affinely related to the score function $\nabla_{x_t} \log q(x_t)$. For discrete data, several noising processes have been considered (Hoogeboom et al., 2021; Austin et al., 2021). The most popular for text is *masked diffusion with an absorbing state*, which progressively randomly masks tokens in the forward process. Another common choice is uniform diffusion, where in the forward process, tokens can flip to any other symbol with some probability depending on the noise level. In both cases, the model learns the posterior $q(x_0|x_t)$ – the discrete analogue of the score.

3 Numerical Experiments

In this section, we present a systematic analysis of the generalization and memorization behaviors of over-parameterized diffusion models across two distinct data modalities: images and text.

3.1 Vision diffusion models

Generalization before memorization We assess the generalization and memorization behaviors of vision diffusion models by considering Improved Denoising Diffusion Probabilistic Models (iDDPMs) (Nichol & Dhariwal, 2021) with a U-Net architecture (Ronneberger et al., 2015; Salimans et al., 2017), including attention blocks (Vaswani et al., 2017). Each model, comprising approximately 0.5B parameters, is trained on four distinct subsets of the CIFAR-10 dataset (Krizhevsky et al., 2009), with training set sizes $P \in \{2048, 4096, 8192, 16384\}$. The models are trained for a total of 262,144 training steps, with full training details in Appendix B.

We track model performance using the diffusion losses on the train set and a validation set of 1,024 images. At regular checkpoints, we generate 32,768 images using each model, and evaluate memorization by calculating the fraction of generated images that are near-exact replicas of training samples. Specifically, following Carlini et al. (2023); Yoon et al. (2023), for a generated image x, we identify the two closest images x' and x'' in Euclidean distance from the training set, and classify x as a copy if $\|x - x'\|_2/\|x - x''\|_2 < 1/3$. This threshold aligns with human perception of visual similarity (Yoon et al., 2023).

Results and analysis Figure 1 (left panel) presents the results of this experiment. Our key findings are as follows:

1. **Generalization before memorization:** Initially, both train and validation loss decrease, indicating that the model is generalizing, i.e., approaching the population score. However, at some critical time τ_{mem}, the two losses bifurcate, signalling the onset of memorization. After this point, the number of copies among generated images steadily increases. By the end of training, all models exhibit some degree of memorization, with copy rates ranging from 1% for the largest training set to 100% for the smaller ones.
2. **Memorization is delayed by larger training sets:** The onset of memorization τ_{mem} scales approximatively linearly with the training set size P, as indicated in the insets of Figure 1.

These observations suggest that early stopping can effectively prevent the model from entering the memorization phase. As a concrete example, the right panel of Figure 1 displays images generated by a diffusion model trained on 16,384 images, with early stopping applied at τ_{mem}. The quality and diversity of these images are quantified using the Fréchet Inception Distance (FID), calculated using Inception v3 against the union of the CIFAR-10 standard train and test splits – a reference set distinct from, and much larger than, the training subset used by the model, so that low FID requires both quality and diversity relative to the population. Along training, the FID decreases as the model learns the population distribution, reaches a minimum at $\tau \approx \tau_{\text{mem}}$, and then grows again as the model enters the memorization phase and loses sample diversity relative to the reference distribution. The early-stopped model achieves an FID score of 5.4, indicating – despite being strongly overparameterized – robust generalization, while the rate of copies is 0%. In Appendix C, we show the same overfitting phenomenon and linear scaling in Stable Diffusion (Rombach et al., 2022) – a text-to-image latent diffusion model – fine-tuned on a subset of the LAION dataset (Schuhmann et al., 2022).

Progressive generalization before memorization We extend our analysis by conducting a second experiment inspired by Kadkhodaie et al. (2023). Specifically, we train two models on two non-overlapping subsets $\mathcal{D}_1$ and $\mathcal{D}_2$ of $2,048$ images of CelebA (Liu et al., 2018), a dataset with faces of celebrities, each using an iDDPM (details in Appendix B). Our setup goes beyond prior work by dynamically tracking the evolution of the generated images throughout training, rather than statically only at convergence (Kadkhodaie et al., 2023). This approach provides a detailed view of how models first approach the population score and then diverge after entering the memorization phase.

Results and analysis We generate samples from both models at multiple checkpoints during training, initializing the generations from the same Gaussian random noise and fixing the stochastic part of the backward trajectories. Remarkably, initially, the images generated by the two models are nearly identical, reflecting that the two models are learning the same score function, even though they are trained on disjoint data subsets. However, at some time τ_{mem}, the models begin to diverge. This divergence coincides with the onset of memorization, where the models start generating images increasingly similar to the ones contained in their respective training sets.

We quantitatively assess this phenomenon using cosine similarity between whitened images generated by the two models and their nearest training images. As shown in Figure 2:

1. **Before memorization** ($\tau < \tau_{\text{mem}}$), the two models generate nearly identical images, indicating that they are dynamically learning the same underlying distribution.

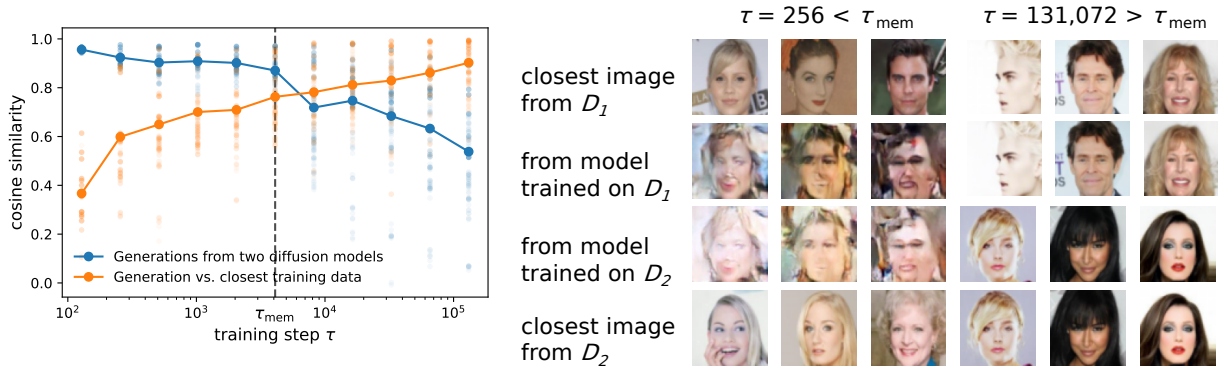

Figure 2: **Progressive generalization in vision diffusion models.** Cosine similarity between images generated by two diffusion models trained on disjoint subsets of CelebA of size $P = 2,048$, as a function of training steps τ. Throughout the pre-memorization window ($\tau < \tau_{\text{mem}}$), the two models generate nearly identical images, indicating they are approximating the same underlying score function – a property of the population distribution and not of the training set used. After τ_{mem}, the models diverge, generating images increasingly similar to their own training sets.

2. **During memorization** ($\tau > \tau_{\text{mem}}$), the similarity between the models' generated images decreases monotonically, while the similarity between each model's generated images and their own training set increases. This reflects the transition from generalization to memorization.

Our findings extend those of Kadkhodaie et al. by revealing that the transition from generalization to memorization is not only a matter of model capacity and final convergence but is dynamically observable throughout training. In practice, this further supports the view that early stopping can prevent the memorization phase and maintain generalization.

3.2 Language diffusion models

We further extend our analysis of generalization and memorization to language data, using MD4, a masked diffusion model specifically designed for text (Shi et al., 2024). Our experiments are conducted on the text8 dataset, a standard benchmark for language modeling based on Wikipedia, with character-level tokenization. To the best of our knowledge, this is the first demonstration of memorization in the masked diffusion language setting. We train MD4 from scratch using a standard GPT-like transformer architecture with approximately 165M parameters. Following the masked diffusion approach, the model is trained to predict masked tokens in noisy text sequences, effectively learning a score function over text data. Full details are presented in Appendix B.

We use training set sizes $P \in \{64, 128, 256, 512, 1024\}$ ranging from 16,384 to

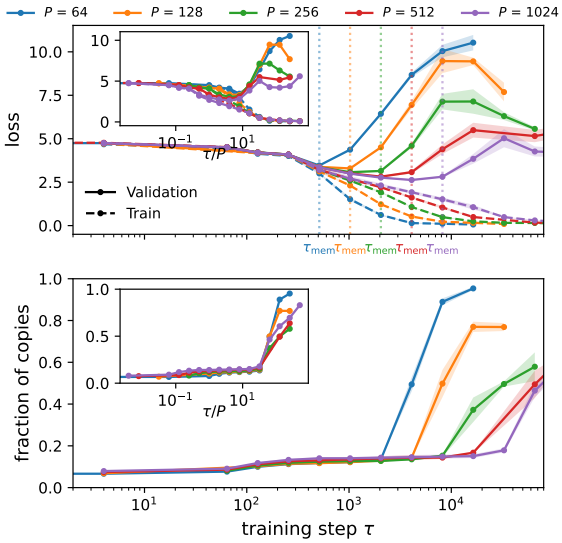

Figure 3: **Memorization dynamics in language diffusion models.** Train and validation loss, validation loss, and fraction of copied text as a function of training steps for GPT-based MD4 models trained on text8 with character-level tokenization and varying training set sizes P. Both losses initially decrease, indicating generalization, but diverge at the onset of memorization (τ_{mem}), where the models start copying training text. τ_{mem} grows linearly with P (insets). Lines: mean across 3 independent runs; shaded bands: ± 1 std.

262,144 tokens. We track model performance using the validation loss on 19,531 sentences, which provides a lower bound to the negative log likelihood, and monitor memorization by generating 1,024 text samples at regular training checkpoints. Memorization is quantified by calculating the Hamming distance between each generated text sample and the closest training set text, averaged over the generations and divided by the sequence length. This metric captures the fraction of exact token matches between the generated and training text.

Results and analysis Figure 3 presents the results of this experiment. As with the vision diffusion models, MD4 initially generalizes, improving the log-likelihood on the validation corpus. However, after τ_{mem} the model begins to produce exact or near-exact copies of training text, signaling the onset of memorization. Notably, τ_{mem} scales linearly with the training set size P, consistent with our previous findings. The transition to memorization is also marked by a sudden increase in the validation loss, indicating that early stopping can effectively prevent memorization also in this setting.

4 Theoretical Analysis: A Competition Between Two Spectral Scales

We have empirically shown that as they train, diffusion models generate higher and higher quality data, which are novel. This is true up to an early stopping time τ_{mem} where memorization starts, which across all image and language diffusion models we tested, follows a strikingly consistent empirical scaling law:

$$\tau_{\text{mem}} \propto P. \tag{1}$$

Training hence exhibits a generalization regime preceding τ_{mem}, whose extensive dependence on P widens this regime as the dataset grows. In this section, we argue that both phenomena – the P-independent emergence of generalization and the P-linear memorization scale – arise in a tractable kernel regime.

Consider the score at noise level σ, $g_\sigma = \nabla_x \log p_\sigma$, where p_σ is the empirical distribution convolved with $\mathcal{N}(0, \sigma^2 I_d)$. Memorization occurs at low diffusion noise: this is the regime in which the backward process collapses onto individual training points (Biroli et al., 2024), and where the empirical score g_σ differs most sharply from its population counterpart $\bar{g}_\sigma$. We therefore work in this low-noise, well-separated regime, where the noise level is much smaller than the typical distance between training points – so that the Gaussian components of p_σ centered at distinct training points have negligible overlap – and consider the decomposition

$$g_\sigma = \bar{g}_\sigma + \xi_\sigma, \qquad \xi_\sigma := g_\sigma - \bar{g}_\sigma. \tag{2}$$

The population score $\bar{g}_\sigma$ is determined by the data distribution and is independent of the particular training sample. The residual ξ_σ encodes which training points were drawn, and has an explicit local form: near each training point, its dominant term is a localized, odd, linear field of magnitude $1/\sigma$, pointing radially inward toward each training example.

Kernel methods and learning timescales We consider the simplified setting where the score is learned by *kernel regression*. Kernel methods admit closed-form analysis and capture neural networks in the lazy regime via the Neural Tangent Kernel (NTK) (Jacot et al., 2018). We work with an isotropic kernel $K(x, y) = \kappa(\|x - y\|)$ and assume the local expansion

$$\kappa(r) = \kappa(0) - C_K r^\nu + O(r^{\nu+\eta}), \tag{3}$$

as $r \to 0$, where ν captures the local regularity of the kernel. The kernel defines an integral operator T_K on the measure p_σ. Under gradient flow, each eigenmode of T_K is learned exponentially fast, with characteristic time set by the inverse of its eigenvalue λ: *large eigenvalues correspond to fast directions, small eigenvalues to slow ones.* The two timescales associated with $\bar{g}_\sigma$ and ξ_σ are therefore determined by where in the spectrum of T_K they sit.

Population score Define the population kernel operator $\bar{T}_K$ on the population distribution $\bar{p}_\sigma$, and expand the population score in its basis. Let λ_{gen} be the smallest eigenvalue it excites.[1] Crucially, λ_{gen} depends on

[1] When $\bar{g}_\sigma$ has spectral weight at arbitrarily small eigenvalues, an analogous statement holds at any fixed accuracy.

the kernel, the noise level, and the data distribution, but not on the training sample – in particular, it is independent of P. This carries over to the empirical operator T_K, whose elements concentrate around those of $\bar{T}_K$ at the standard rate $P^{-1/2}$, so the empirical eigenvalues on the population modes converge to their population values, and in particular remain $\Theta(1)$ as $P \to \infty$. Thus, $\tau_{\text{gen}} \sim 1/\lambda_{\text{gen}}$, *independent of* P.

Scorelets and the memorization timescale We now identify the spectral scale of the localized residual. For each training point x_i and unit vector $u \in \mathbb{S}^{d-1}$, define a *scorelet* as

$$\phi_{i,u}(x) = u^\top (x - x_i)\, R\left(\frac{\|x - x_i\|}{\sigma}\right), \tag{4}$$

where R is a smooth, compactly supported radial cutoff. By construction, the scorelet $\phi_{i,u}$ has the same structure as the local residual field – localized, odd, and linear near x_i – and is therefore the natural test function to detect the spectral location of the modes responsible for memorization. We then compute the *Rayleigh quotient* of $\phi_{i,u}$ against K,

$$\mathcal{R}_{i,u}(\sigma, P) := \frac{\langle \phi_{i,u}, T_K \phi_{i,u} \rangle}{\|\phi_{i,u}\|^2}. \tag{5}$$

The Rayleigh quotient is a weighted average of the eigenvalues of T_K excited by $\phi_{i,u}$. In particular, its inverse is a *lower bound* on the slowest eigen-timescale present in the scorelet direction. Its leading-order behavior is given by the following.

Proposition 1 (informal, see Proposition 2)**.** *For an isotropic kernel with local expansion Equation 3, in the low-noise regime, for every training point x_i and every unit vector u,*

$$\mathcal{R}_{i,u}(\sigma, P) = C\,\frac{\sigma^\nu}{P} + O\left(\frac{\sigma^{\nu+\eta}}{P}\right), \tag{6}$$

for a kernel- and dimension-dependent constant $C > 0$.

Intuitively, the empirical density p_σ is a mixture of P Gaussian bumps centered at the training points, each carrying mass $1/P$. The residual field at each x_i is supported on its bump, and this $1/P$ weight pushes the eigenvalues of the corresponding modes down to the spectral scale σ^ν/P, whose inverse gives the memorization timescale

$$\tau_{\text{mem}} \gtrsim \frac{P}{\sigma^\nu}, \tag{7}$$

linear in P, consistent with the empirical scaling Equation 1. This generalizes the random-feature result of Bonnaire et al. (2025) to any isotropic kernel, and reveals that the memorization timescale depends on the local regularity of the kernel. For instance, ReLU NTK ($\nu = 1$) and random-feature kernels ($\nu = 2$) have different σ-dependence.

The generalization window Combining the two scales yields, for any fixed noise level σ, a window $\tau_{\text{gen}} \ll \tau \ll \tau_{\text{mem}}$ that grows linearly in P. Inside this window, the kernel has learned the population component of the score but has not yet fit the local structure encoded in the scorelet directions. In other words, generalization is governed by modes with P-stable eigenvalues, memorization is governed by the localized residual modes, whose eigenvalues become smaller and smaller as P grows.

Numerical confirmation We confirm the predicted scaling with both P and σ in Proposition 1 numerically using one-hidden-layer networks in the Neural Tangent Kernel (NTK) regime (Jacot et al., 2018) (Figure 15), indicating that the lower bound is tight up to constants. Interestingly, the same scaling holds under feature-learning initialization (Figure 16), suggesting that the mechanism extends beyond the fixed-kernel assumption.

The kernel argument predicts a memorization timescale set by the spectrum of T_K alone. Empirically, this scale is reached at the same number of steps regardless of optimization details: τ_{mem} is essentially unchanged from small-batch SGD to full-batch GD (Figure 17). Thus, contrary to a possible intuition that memorization

should depend on the number of times each example is revisited, the total number of optimization steps is what matters. Similarly, adaptive optimizers like Adam shift τ_{mem} by only a constant factor while preserving the linear scaling in P (Figure 18).

We will now study a controlled model of synthetic data that captures the phenomenology observed for natural data. Most importantly, it will allow us to quantify in detail the inaccuracy of generations of diffusion models with limited training, responsible for the inconsistent images in Figure 2.

5 Generalization vs. Memorization with a Simple Grammar

In this section, we consider diffusion models trained to generate sentences respecting the rules of a simple formal grammar, which gives a theoretical framework to interpret the generalization-memorization dynamics in real data.

5.1 Probabilistic graphical models

In theoretical linguistics, *Probabilistic Context-Free Grammars* (PCFG) have been proposed as a framework to describe the hierarchical structure of the syntax of several languages (Chomsky, 1956; Rozenberg & Salomaa, 1997; Pullum & Gazdar, 1982; Joshi, 1985; Manning & Schütze, 1999). Moreover, they have been proposed for describing semantic aspects of images under the name of *Pattern Theory* (Grenander, 1996; Jin & Geman, 2006; Siskind et al., 2007). PCFGs consist of a vocabulary of latent (*nonterminal*) symbols and a vocabulary of visible (*terminal*) symbols, together with probabilistic *production rules* establishing how one latent symbol generates tuples of symbols.

The Random Hierarchy Model (RHM) The RHM (Cagnetta et al., 2024) is a simple PCFG introduced as a theoretical toy model describing hierarchy and compositionality in data. With respect to generic PCFGs, it is built with some simplifying assumptions:

- Symbols are organized in a regular-tree topology of depth L and branching factor s. The bottom layer, indexed as $\ell = 0$, corresponds to the leaves of the tree, which are the visible (terminal) symbols. The upper part of the tree, with layers $\ell = 1, \dots, L$, corresponds to latent (nonterminal) symbols in the data structure.
- Nonterminal symbols are taken from L finite vocabularies $(\mathcal{V}_\ell)_{\ell=1,\dots,L}$ of size v for each layer $\ell = 1, \dots, L$. Terminal symbols belong to the vocabulary $\mathcal{V} \equiv \mathcal{V}_0$ of size v.
- The production rules transform one symbol in a node at level $\ell + 1$ into a string of s symbols in its children nodes at level ℓ. For each non-terminal symbol, there are m rules with equal probability, which are *unambiguous*, i.e., two distinct symbols cannot generate the same s-string. Rules are sampled randomly without replacement and frozen for a given instance of the RHM. The m strings generated by the same latent symbol are referred to as *synonyms*.

The fixed tree topology ensures that visible data at the leaves are strings of fixed length $d = s^L$. In analogy with language modeling, we call visible symbols *tokens*.

The number of possible data generated by this model is $vm^{\frac{d-1}{s-1}}$, which is exponential in the data dimension. Because of the random production rules, the tokens of the RHM data have non-trivial correlations reflecting the latent hierarchical structure (Cagnetta & Wyart, 2024).

5.2 Diffusion on the Random Hierarchy Model

The exact score function of the RHM Because of its correlations, the probability distribution of the RHM data and its corresponding score function are highly non-trivial. Nevertheless, if the production rules are known, thanks to the latent tree structure, the score function for any noise level can be computed exactly using the Belief Propagation (BP) algorithm. (Mezard & Montanari, 2009).

Sample complexity Favero et al. (2025) studied the sample complexity for diffusion models based on deep neural networks trained on finite RHM data. Their main findings are the following.

- The sample complexity to learn to generate valid data depends on the parameters of the model as $P^* \sim vm^{L+1}$, which is polynomial in the dimension, i.e., $P^* \sim vmd^{\log m/\log s}$. This scale can be theoretically predicted by comparing the size of the correlations between tokens and latent features, used in deep architectures for denoising, with their sampling noise.
- For $P < P^*$, there are regimes of partial generalization where the generated data are consistent with the rules up to layer ℓ. The sample complexity to learn the rules at layer ℓ scales as $P^*_\ell \sim vm^{\ell+1}$.
- When $P > P^*_\ell$, the number of training steps τ^*_ℓ required to learn the rules at layer ℓ is proportional to P^*_ℓ, therefore having the same polynomial scaling with the dimension. Complete generalization is therefore achieved with $\tau^* \propto P^* = P^*_L$ number of training steps.

Notice that the sample complexity depends on the underlying distribution, e.g., the parameters of the grammar, and not on the specific number of available training samples.

5.3 Generalization vs. memorization

We consider an instantiation of the RHM with a given set of parameters (depth L, branching factor s, vocabulary size v, and number of synonyms m). We generate P distinct strings from this grammar, which constitute the training set. Each token is one-hot encoded, and we train a *Discrete Denoising Diffusion Probabilistic Model* (D3PM) (Austin et al., 2021) with uniform transition probabilities (Hoogeboom et al., 2021). The architecture of the diffusion model is made of a convolutional U-Net (Ronneberger et al., 2015) with $2L$ layers in total – L in the encoder and L in the decoder. We consider highly overparameterized networks with 8,192 channels per layer, with a total number of parameters varying between 0.4B for $L = 3$ and 0.7B for $L = 5$. We use the maximal-update (μP) initialization to ensure feature learning (Yang & Hu, 2020). We train the neural network using Adam to optimize the training loss of discrete diffusion (Austin et al., 2021), derived from a variational bound on the negative log-likelihood (Sohl-Dickstein et al., 2015). Further experimental details are reported in Appendix B.

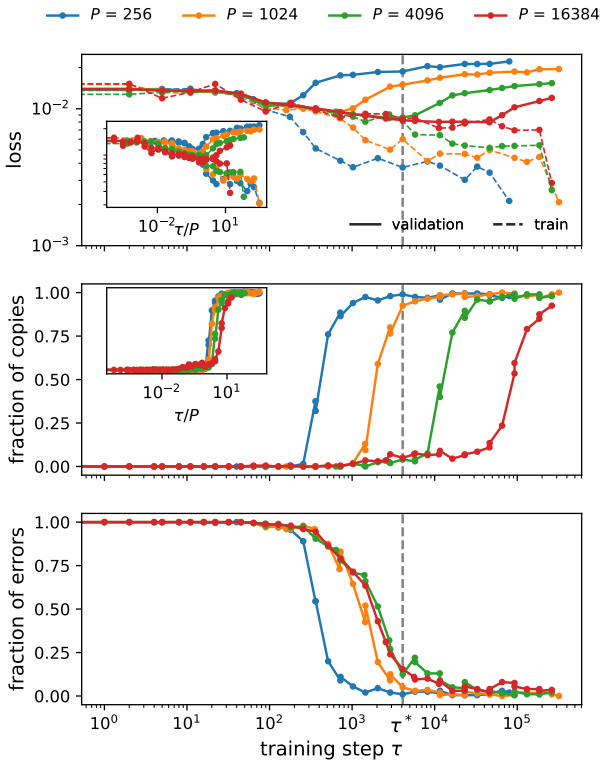

Figure 4: **Memorization vs. generalization on the RHM.** For training set size $P = 256$, the diffusion model generates valid data only when it is memorizing For $P = 16{,}384$, instead, the model generalizes, approximately at τ^*, before starting to memorize. The memorization time scales linearly in P (insets). Data for RHM parameters $v = 16$, $m = 4$, $L = 3$, $s = 2$.

We study the evolution of the models during training. For checkpoints at different training times, we track the training loss and the validation loss on 2,048 held-out data. In addition, we generate 1,024 data points with the diffusion model and measure their Hamming distance with the training data, determining if they are copies or not. We also check if the generated data are compatible with all the rules of the RHM, determining if they are valid strings of the grammar or not.

Results and analysis Figure 4 shows the evolution of a diffusion model during training with RHM parameters $v = 16$, $m = 4$, $L = 3$, $s = 2$. For these parameters, the sample complexity to learn all the rules

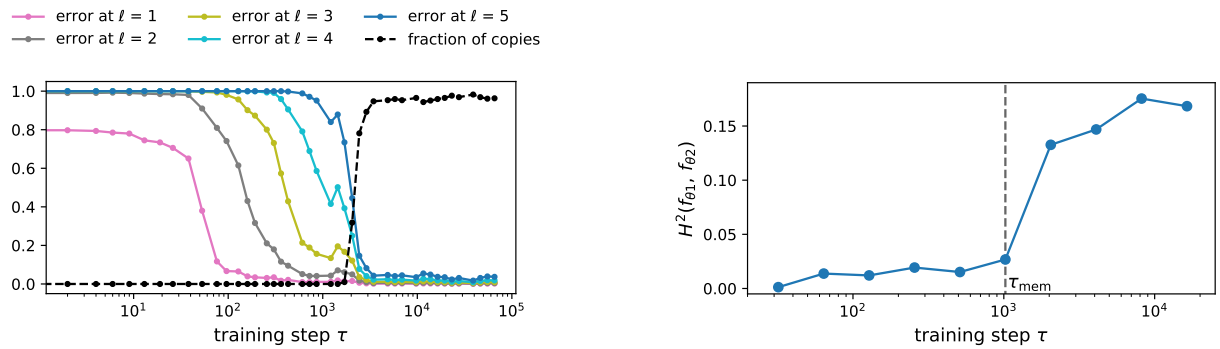

(a) Layer-wise learning in the RHM before memorization.

(b) Distance between the outputs of two diffusion models trained on disjoint training sets.

Figure 5: **Diffusion models achieve partial generalization in the RHM before memorizing.** (a) The diffusion model learns progressively deeper RHM rules during training. However, the rules at the deepest level $L = 5$ are never learned, and the corresponding error decreases only when memorization occurs, since $P = 1{,}024$ is smaller than the sample complexity $P_L^* \sim 10^4$. (b) Two diffusion models trained on disjoint training sets learn the same score function before the onset of memorization at τ_{mem}. Data for RHM parameters $v = 16$, $m = 3$, $L = 5$, $s = 2$.

of the grammar is $P^* \approx 4{,}096$. Varying the training set size P, we observe that the validation and training losses start decreasing at the same time and follow the same behavior until separating later in training, at a time depending on P. Comparing these losses with the fraction of copies between the generated data and the training ones, we observe that the increase of the validation loss corresponds to the onset of memorization. As observed for real data in section 3, we find empirically that the onset of memorization requires a number of training steps τ_{mem} proportional to P (insets of Figure 4). The fraction of errors measures how many of the generated data are not compatible with the RHM rules. We observe that for $P < 4{,}096$, the fraction of errors decreases only in correspondence with memorization: the generated data are valid according to the grammar rules, but they are copies of the training set. For $P > 4{,}096$, instead, the fraction of errors decreases *before* the onset of memorization: the diffusion model is generating valid data that do not belong to the training set, and it is therefore generalizing. In Appendix F, we show that the generated data respect the correct statistics of the RHM rules, therefore learning the true data distribution. As a reference, Figure 4 reports the time $\tau^* = P^*$ as a vertical dashed line. We observe that the generalizing models ($P = 4{,}096$ and $P = 16{,}384$) achieve a fraction of errors $< 15\%$ for $\tau > \tau^*$. Therefore, these models present a dynamical phase $\tau^* < \tau < \tau_{\text{mem}}$ where they achieve nearly perfect generalization before starting to memorize. This phase becomes longer with increasing P.

5.4 Partial generalization

For $P < P^*$, the diffusion model does not have enough training data to learn the deeper levels of the rules. However, it can still learn the lower levels of the rules up to layer $\tilde{\ell}$, with $P > P_{\tilde{\ell}}^*$, as the sample complexity P_ℓ^* increases with ℓ. In this case, the model achieves *partial generalization*, corresponding to learning to generate data with some local coherence but lacking a global one, consistent with observations of Figure 2.

In Figure 5(a), a diffusion model is trained with $P = 1{,}024$ training points of an RHM with depth $L = 5$, while the sample complexity to learn all the rules is $P^* = P_L^* \simeq 10^4$. During training, we generate data with the diffusion model and measure if they are compatible with the RHM rules at layer ℓ, measuring the corresponding fraction of errors. The figure shows that the errors at the layers $\ell \leq 3$ decrease at training times depending on ℓ, in accordance with $\tau_\ell \propto P_\ell^*$ (Favero et al., 2025). However, for $\ell > 3$, the fractions of errors reach small values only at the onset of memorization τ_{mem}, when the fraction of copies of the training set goes up. This behavior implies that the model never learns the rules at the deeper levels $\ell = 4, 5$ since the

number of training data is smaller than the sample complexity, and generates data with global consistency only when it starts memorizing.

Even when partially generalizing, diffusion models learn the same score function Even without achieving perfect generalization, diffusion models gradually improve their generalization during training – before memorizing – by capturing some structure of the underlying data distribution. In the RHM case, this corresponds to the lowest levels of the grammar. As a consequence, the score function that is learned during training *before memorization* is the same *independently* of the sampling of the training set. In Figure 5(b), we train two diffusion models in the same setting as Figure 5(a) but with two disjoint training sets. We measure the difference in their outputs – i.e., the components of the learned score – during training by computing their Hellinger distance, defined as $H(p,q) = 2^{-1/2}\sqrt{\sum_{i=1}^{v}(\sqrt{p_i}-\sqrt{q_i})^2}$, with $p = (p_i)_{i\in[v]}$ and $q = (q_i)_{i\in[v]}$ two discrete probability distributions; this distance is averaged over the tokens and the sampling of the diffusion trajectories from 1,024 test data. We observe that the distance between the output functions of the two models, i.e., the learned scores – which determine the generative process – remains stable during training and only jumps to higher values when the models start memorizing their respective training sets. Therefore, the two diffusion models learn very similar score functions when their generalization is gradually improving, before they overfit their respective empirical scores.

6 Related work

Memorization in diffusion models Several works have documented the tendency of diffusion models to memorize the training data (Carlini et al., 2023; Somepalli et al., 2022; 2023; Wang et al., 2024). Dockhorn et al. (2022) proposes a mitigation strategy based on differentially private stochastic gradient descent, while Chen et al. (2024) introduces an anti-memorization guidance. Yoon et al. (2023); Kadkhodaie et al. (2023); Gu et al. (2025) interpret memorization as an overfitting phenomenon driven by the large capacity of overparameterized neural networks. Kadkhodaie et al. (2023) shows that underparameterized models trained on disjoint training sets learn the same score function, therefore generalizing by sampling the same target distribution; in contrast, overparameterized models memorize. Li et al. (2024); Wang & Vastola (2024) find that during their initial training phases, overparameterized diffusion models have an inductive bias towards learning a Gaussian approximation of data. This process achieves a primitive form of partial generalization by capturing some data's low-dimensional structure before the model begins to fully memorize the training points. Our results extend this viewpoint to later training stages and higher-order data statistics. Additionally, we quantify the timescale at which models transition from generalizing to memorizing.

Overfitting in supervised learning vs. diffusion models Although the dynamics of first generalizing and then overfitting to the training data is observed also in some supervised learning settings (Advani et al., 2020; Nakkiran et al., 2021) – where recent theoretical progress has been made (Montanari & Urbani, 2025) – these problems have fundamental differences with memorization in diffusion models, i.e., learning the empirical score. For instance, in a typical regression task, a model fits a target function whose observations are assumed to be corrupted by external, unstructured noise. In the diffusion context, instead, the empirical score at low noise levels significantly differs from the population one: the corresponding "noise", i.e., the difference between the two functions, is inherent to the training set, structured, and defined over the entire domain of the inputs x_t. An overparameterized model converging to the empirical target, therefore, memorizes the training set and cannot generalize. This contrasts with noisy regression, where overparameterization can surprisingly be beneficial, leading to *double descent* (Spigler et al., 2019; Belkin et al., 2019) and *benign overfitting* (Bartlett et al., 2020).

Concurrent work on dynamical regularization Bonnaire et al. (2025) independently and concurrently investigate the role of training dynamics in the memorization-generalization transition of diffusion models. On the empirical side, both works document the same phenomenon: a generalization phase preceding memorization, with $\tau_{\text{mem}} \propto P$. While their numerical experiments primarily focus on CelebA images and U-Nets, our analysis spans a significantly broader range of datasets, data modalities (including language), architectures (including SOTA transformers and latent diffusion models), and diffusion processes (both continuous

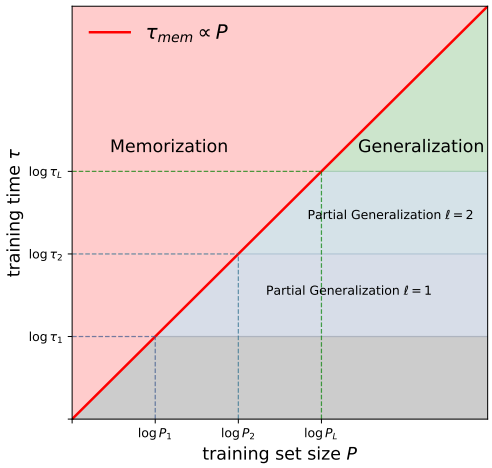

Figure 6: **Phase diagram of generalization vs. memorization** indicating different regimes as a function of training time τ and sample complexity P: partial generalization, (full) generalization and memorization. Note that in the RHM, learning proceeds through well-defined steps, while it is smoother for natural data (or more realistic versions of the RHM (Cagnetta et al., 2025)).

and discrete). On the theoretical side, Bonnaire et al. (2025) provide an asymptotic analysis of random features in the high-dimensional limit. Our spectral argument applies instead to general isotropic kernels. This broader scope reveals that the memorization timescale depends on the local regularity of the kernel, and for instance, differs for random features and the ReLU NTK. Another distinctive aspect of our work is the study of diffusion models learning a context-free grammar (via the RHM), which provides a controlled setting where partial generalization has a precise statistical meaning allowing us to characterize its interplay with memorization through the phase diagram of Figure 6.

7 Conclusion

We have argued that the learning dynamics in diffusion models is best understood as a competition between time scales, as summarized in Figure 6. A larger training set implies a larger memorization time, thus opening a larger time window to generate more coherent data. These results provide a principled handle on the verbatim regeneration of training data, with direct implications for privacy and for mitigating training-data extraction: using early stopping to avoid memorization, and building backward flows that are nearly independent of the specific realization of the training set, as we demonstrated.

References

Beatrice Achilli, Enrico Ventura, Gianluigi Silvestri, Bao Pham, Gabriel Raya, Dmitry Krotov, Carlo Lucibello, and Luca Ambrogioni. Losing dimensions: Geometric memorization in generative diffusion. *arXiv preprint arXiv:2410.08727*, 2024.

Beatrice Achilli, Luca Ambrogioni, Carlo Lucibello, Marc Mézard, and Enrico Ventura. Memorization and generalization in generative diffusion under the manifold hypothesis. *arXiv preprint arXiv:2502.09578*, 2025.

Madhu S. Advani, Andrew M. Saxe, and Haim Sompolinsky. High-dimensional dynamics of generalization error in neural networks. *Neural Networks*, September 2020. ISSN 0893-6080. doi: 10.1016/j.neunet.2020.08.022.

Amira Alakhdar, Barnabas Poczos, and Newell Washburn. Diffusion models in de novo drug design. *Journal of Chemical Information and Modeling*, 64(19):7238–7256, 2024.

Luca Ambrogioni. The statistical thermodynamics of generative diffusion models. *arXiv preprint arXiv:2310.17467*, 2023.

Jacob Austin, Daniel D Johnson, Jonathan Ho, Daniel Tarlow, and Rianne Van Den Berg. Structured denoising diffusion models in discrete state-spaces. *Advances in Neural Information Processing Systems*, 34:17981–17993, 2021.

Peter L Bartlett, Philip M Long, Gábor Lugosi, and Alexander Tsigler. Benign overfitting in linear regression. *Proceedings of the National Academy of Sciences*, 117(48):30063–30070, 2020.

Mikhail Belkin, Daniel Hsu, Siyuan Ma, and Soumik Mandal. Reconciling modern machine-learning practice and the classical bias–variance trade-off. *Proceedings of the National Academy of Sciences*, 116(32):15849–15854, 2019.

Giulio Biroli and Marc Mézard. Generative diffusion in very large dimensions. *arXiv preprint arXiv:2306.03518*, 2023.

Giulio Biroli, Tony Bonnaire, Valentin de Bortoli, and Marc Mézard. Dynamical regimes of diffusion models, 2024.

Andreas Blattmann, Tim Dockhorn, Sumith Kulal, Daniel Mendelevitch, Maciej Kilian, Dominik Lorenz, Yam Levi, Zion English, Vikram Voleti, Adam Letts, et al. Stable video diffusion: Scaling latent video diffusion models to large datasets. *arXiv preprint arXiv:2311.15127*, 2023.

Adam Block, Youssef Mroueh, and Alexander Rakhlin. Generative modeling with denoising auto-encoders and langevin sampling. *arXiv preprint arXiv:2002.00107*, 2020.

Tony Bonnaire, Raphaël Urfin, Giulio Biroli, and Marc Mézard. Why diffusion models don't memorize: The role of implicit dynamical regularization in training. *arXiv preprint arXiv:2505.17638*, 2025.

Francesco Cagnetta and Matthieu Wyart. Towards a theory of how the structure of language is acquired by deep neural networks. In *The Thirty-eighth Annual Conference on Neural Information Processing Systems*, 2024.

Francesco Cagnetta, Leonardo Petrini, Umberto M. Tomasini, Alessandro Favero, and Matthieu Wyart. How deep neural networks learn compositional data: The random hierarchy model. *Phys. Rev. X*, 14:031001, Jul 2024. doi: 10.1103/PhysRevX.14.031001.

Francesco Cagnetta, Hyunmo Kang, and Matthieu Wyart. Learning curves theory for hierarchically compositional data with power-law distributed features. *arXiv preprint arXiv:2505.07067*, 2025.

Nicolas Carlini, Jamie Hayes, Milad Nasr, Matthew Jagielski, Vikash Sehwag, Florian Tramer, Borja Balle, Daphne Ippolito, and Eric Wallace. Extracting training data from diffusion models. In *32nd USENIX Security Symposium (USENIX Security 23)*, pp. 5253–5270, 2023.

Chen Chen, Daochang Liu, and Chang Xu. Towards memorization-free diffusion models. In *Proceedings of the IEEE/CVF Conference on Computer Vision and Pattern Recognition*, pp. 8425–8434, 2024.

Lenaic Chizat, Edouard Oyallon, and Francis Bach. On lazy training in differentiable programming. In *Advances in Neural Information Processing Systems*, pp. 2937–2947, 2019.

Noam Chomsky. Three models for the description of language. *IRE Transactions on information theory*, 2 (3):113–124, 1956.

Hugo Cui, Florent Krzakala, Eric Vanden-Eijnden, and Lenka Zdeborová. Analysis of learning a flow-based generative model from limited sample complexity. *arXiv preprint arXiv:2310.03575*, 2023.

Prafulla Dhariwal and Alexander Nichol. Diffusion models beat gans on image synthesis. *Advances in neural information processing systems*, 34:8780–8794, 2021.

Tim Dockhorn, Tianshi Cao, Arash Vahdat, and Karsten Kreis. Differentially private diffusion models. *arXiv preprint arXiv:2210.09929*, 2022.

Alessandro Favero, Antonio Sclocchi, Francesco Cagnetta, Pascal Frossard, and Matthieu Wyart. How compositional generalization and creativity improve as diffusion models are trained. *arXiv preprint arXiv:2502.12089*, 2025.

Jérôme Garnier-Brun, Marc Mézard, Emanuele Moscato, and Luca Saglietti. How transformers learn structured data: insights from hierarchical filtering. *arXiv preprint arXiv:2408.15138*, 2024.

Anand Jerry George, Rodrigo Veiga, and Nicolas Macris. Denoising score matching with random features: Insights on diffusion models from precise learning curves. *arXiv preprint arXiv:2502.00336*, 2025.

Ulf Grenander. *Elements of pattern theory*. JHU Press, 1996.

Xiangming Gu, Chao Du, Tianyu Pang, Chongxuan Li, Min Lin, and Ye Wang. On memorization in diffusion models. *Transactions on Machine Learning Research*, 2025. ISSN 2835-8856.

Yinbin Han, Meisam Razaviyayn, and Renyuan Xu. Neural network-based score estimation in diffusion models: Optimization and generalization. *arXiv preprint arXiv:2401.15604*, 2024.

Jonathan Ho, Ajay Jain, and Pieter Abbeel. Denoising diffusion probabilistic models. *Advances in neural information processing systems*, 33:6840–6851, 2020.

Jonathan Ho, Tim Salimans, Alexey Gritsenko, William Chan, Mohammad Norouzi, and David J Fleet. Video diffusion models. *Advances in Neural Information Processing Systems*, 35:8633–8646, 2022.

Emiel Hoogeboom, Didrik Nielsen, Priyank Jaini, Patrick Forré, and Max Welling. Argmax flows and multinomial diffusion: Learning categorical distributions. *Advances in Neural Information Processing Systems*, 34:12454–12465, 2021.

Hailong Hu and Jun Pang. Membership inference of diffusion models. *arXiv preprint arXiv:2301.09956*, 2023.

Arthur Jacot, Franck Gabriel, and Clément Hongler. Neural tangent kernel: Convergence and generalization in neural networks. *Advances in Neural Information Processing Systems*, 31:8580–8589, 2018.

Ya Jin and Stuart Geman. Context and hierarchy in a probabilistic image model. In *2006 IEEE computer society conference on computer vision and pattern recognition (CVPR'06)*, volume 2, pp. 2145–2152. IEEE, 2006.

Aravind K. Joshi. Tree adjoining grammars: How much context-sensitivity is required to provide reasonable structural descriptions? In David R. Dowty, Lauri Karttunen, and Arnold M. Zwicky (eds.), *Natural Language Parsing: Psychological, Computational, and Theoretical Perspectives*, pp. 206–250. Cambridge Univ. Press, Cambridge, UK, 1985.

Zahra Kadkhodaie, Florentin Guth, Eero P Simoncelli, and Stéphane Mallat. Generalization in diffusion models arises from geometry-adaptive harmonic representations. *arXiv preprint arXiv:2310.02557*, 2023.

Mason Kamb and Surya Ganguli. An analytic theory of creativity in convolutional diffusion models. *arXiv preprint arXiv:2412.20292*, 2024.

Alex Krizhevsky, Geoffrey Hinton, et al. Learning multiple layers of features from tiny images. 2009.

Marvin Li and Sitan Chen. Critical windows: non-asymptotic theory for feature emergence in diffusion models. In *International Conference on Machine Learning*, pp. 27474–27498. PMLR, 2024.

Puheng Li, Zhong Li, Huishuai Zhang, and Jiang Bian. On the generalization properties of diffusion models. *Advances in Neural Information Processing Systems*, 36:2097–2127, 2023.

Xiang Li, Yixiang Dai, and Qing Qu. Understanding generalizability of diffusion models requires rethinking the hidden gaussian structure. *Advances in neural information processing systems*, 37:57499–57538, 2024.

Ziwei Liu, Ping Luo, Xiaogang Wang, and Xiaoou Tang. Large-scale celebfaces attributes (celeba) dataset. *Retrieved August*, 15(2018):11, 2018.

Christopher D. Manning and Hinrich Schütze. *Foundations of Statistical Natural Language Processing*. MIT Press, Cambridge, MA, 1999. doi: 10.7551/mitpress/10438.001.0001.

Tomoya Matsumoto, Takayuki Miura, and Naoto Yanai. Membership inference attacks against diffusion models. In *2023 IEEE Security and Privacy Workshops (SPW)*, pp. 77–83. IEEE, 2023.

Song Mei. U-nets as belief propagation: Efficient classification, denoising, and diffusion in generative hierarchical models. *arXiv preprint arXiv:2404.18444*, 2024.

Song Mei, Andrea Montanari, and Phan-Minh Nguyen. A mean field view of the landscape of two-layer neural networks. *Proceedings of the National Academy of Sciences*, 115(33):E7665–E7671, August 2018. ISSN 0027-8424, 1091-6490. doi: 10.1073/pnas.1806579115. Publisher: National Academy of Sciences Section: PNAS Plus.

Marc Mezard and Andrea Montanari. *Information, physics, and computation*. Oxford University Press, 2009.

Andrea Montanari and Pierfrancesco Urbani. Dynamical decoupling of generalization and overfitting in large two-layer networks. *arXiv preprint arXiv:2502.21269*, 2025.

Preetum Nakkiran, Gal Kaplun, Yamini Bansal, Tristan Yang, Boaz Barak, and Ilya Sutskever. Deep double descent: Where bigger models and more data hurt. *Journal of Statistical Mechanics: Theory and Experiment*, 2021(12):124003, 2021.

Alexander Quinn Nichol and Prafulla Dhariwal. Improved denoising diffusion probabilistic models. In *International Conference on Machine Learning*, pp. 8162–8171. PMLR, 2021.

Shen Nie, Fengqi Zhu, Zebin You, Xiaolu Zhang, Jingyang Ou, Jun Hu, Jun Zhou, Yankai Lin, Ji-Rong Wen, and Chongxuan Li. Large language diffusion models. *arXiv preprint arXiv:2502.09992*, 2025.

Kazusato Oko, Shunta Akiyama, and Taiji Suzuki. Diffusion models are minimax optimal distribution estimators. *arXiv preprint arXiv:2303.01861*, 2023.

Ed Pizzi, Sreya Dutta Roy, Sugosh Nagavara Ravindra, Priya Goyal, and Matthijs Douze. A self-supervised descriptor for image copy detection. In *Proceedings of the IEEE/CVF Conference on Computer Vision and Pattern Recognition*, pp. 14532–14542, 2022.

Geoffrey K. Pullum and Gerald Gazdar. Natural languages and context-free languages. *Linguist. Philos.*, 4 (4):471–504, 1982. doi: 10.1007/BF00360802.

Aditya Ramesh, Prafulla Dhariwal, Alex Nichol, Casey Chu, and Mark Chen. Hierarchical text-conditional image generation with clip latents. *arXiv preprint arXiv:2204.06125*, 1(2):3, 2022.

Robin Rombach, Andreas Blattmann, Dominik Lorenz, Patrick Esser, and Björn Ommer. High-resolution image synthesis with latent diffusion models. In *Proceedings of the IEEE/CVF conference on computer vision and pattern recognition*, pp. 10684–10695, 2022.

Olaf Ronneberger, Philipp Fischer, and Thomas Brox. U-net: Convolutional networks for biomedical image segmentation. In *Medical image computing and computer-assisted intervention–MICCAI 2015: 18th international conference, Munich, Germany, October 5-9, 2015, proceedings, part III 18*, pp. 234–241. Springer, 2015.

Grzegorz Rozenberg and Arto Salomaa. *Handbook of Formal Languages*. Springer, January 1997. doi: 10.1007/978-3-642-59126-6.

Subham Sekhar Sahoo, Marianne Arriola, Yair Schiff, Aaron Gokaslan, Edgar Marroquin, Justin T Chiu, Alexander Rush, and Volodymyr Kuleshov. Simple and effective masked diffusion language models. *arXiv preprint arXiv:2406.07524*, 2024.

Tim Salimans, Andrej Karpathy, Xi Chen, and Diederik P Kingma. Pixelcnn++: Improving the pixelcnn with discretized logistic mixture likelihood and other modifications. *arXiv preprint arXiv:1701.05517*, 2017.

Christoph Schuhmann, Romain Beaumont, Richard Vencu, Cade Gordon, Ross Wightman, Mehdi Cherti, Theo Coombes, Aarush Katta, Clayton Mullis, Mitchell Wortsman, et al. Laion-5b: An open large-scale dataset for training next generation image-text models. *Advances in neural information processing systems*, 35:25278–25294, 2022.

Antonio Sclocchi, Alessandro Favero, Noam Itzhak Levi, and Matthieu Wyart. Probing the latent hierarchical structure of data via diffusion models. *arXiv preprint arXiv:2410.13770*, 2024a.

Antonio Sclocchi, Alessandro Favero, and Matthieu Wyart. A phase transition in diffusion models reveals the hierarchical nature of data. *arXiv preprint arXiv:2402.16991*, 2024b.

Kulin Shah, Sitan Chen, and Adam Klivans. Learning mixtures of gaussians using the ddpm objective. *Advances in Neural Information Processing Systems*, 36:19636–19649, 2023.

Jiaxin Shi, Kehang Han, Zhe Wang, Arnaud Doucet, and Michalis K Titsias. Simplified and generalized masked diffusion for discrete data. *arXiv preprint arXiv:2406.04329*, 2024.

Jeffrey Mark Siskind, J Sherman, Ilya Pollak, Mary P Harper, and Charles A Bouman. Spatial random tree grammars for modeling hierarchal structure in images with regions of arbitrary shape. *IEEE Transactions on Pattern Analysis and Machine Intelligence*, 29(9):1504–1519, 2007.

Jascha Sohl-Dickstein, Eric Weiss, Niru Maheswaranathan, and Surya Ganguli. Deep unsupervised learning using nonequilibrium thermodynamics. In *International conference on machine learning*, pp. 2256–2265. PMLR, 2015.

G Somepalli, V Singla, M Goldblum, J Geiping, and T Goldstein. Diffusion art or digital forgery. *Investigating Data Replication in Diffusion Models*, 2022.

Gowthami Somepalli, Vasu Singla, Micah Goldblum, Jonas Geiping, and Tom Goldstein. Understanding and mitigating copying in diffusion models. *Advances in Neural Information Processing Systems*, 36: 47783–47803, 2023.

Yang Song and Stefano Ermon. Generative modeling by estimating gradients of the data distribution. *Advances in neural information processing systems*, 32, 2019.

Yang Song, Jascha Sohl-Dickstein, Diederik P Kingma, Abhishek Kumar, Stefano Ermon, and Ben Poole. Score-based generative modeling through stochastic differential equations. *arXiv preprint arXiv:2011.13456*, 2020.

S. Spigler, M. Geiger, S. d'Ascoli, L. Sagun, G. Biroli, and M. Wyart. A jamming transition from under- to over-parametrization affects generalization in deep learning. *Journal of Physics A: Mathematical and Theoretical*, 52(47):474001, October 2019. ISSN 1751-8121. doi: 10.1088/1751-8121/ab4c8b. Publisher: IOP Publishing.

Ashish Vaswani, Noam Shazeer, Niki Parmar, Jakob Uszkoreit, Llion Jones, Aidan N Gomez, Lukasz Kaiser, and Illia Polosukhin. Attention is All you Need. In *Advances in Neural Information Processing Systems*, volume 30. Curran Associates, Inc., 2017.

Nikhil Vyas, Sham M Kakade, and Boaz Barak. On provable copyright protection for generative models. In *International conference on machine learning*, pp. 35277–35299. PMLR, 2023.

Binxu Wang and John J Vastola. The unreasonable effectiveness of gaussian score approximation for diffusion models and its applications. *arXiv preprint arXiv:2412.09726*, 2024.

Wenhao Wang, Yifan Sun, Zongxin Yang, Zhengdong Hu, Zhentao Tan, and Yi Yang. Replication in visual diffusion models: A survey and outlook. *CoRR*, 2024.

Joseph L Watson, David Juergens, Nathaniel R Bennett, Brian L Trippe, Jason Yim, Helen E Eisenach, Woody Ahern, Andrew J Borst, Robert J Ragotte, Lukas F Milles, et al. De novo design of protein structure and function with rfdiffusion. *Nature*, 620(7976):1089–1100, 2023.

Yixin Wu, Ning Yu, Zheng Li, Michael Backes, and Yang Zhang. Membership inference attacks against text-to-image generation models. *arXiv preprint arXiv:2210.00968*, 2022.

Greg Yang and Edward J Hu. Feature learning in infinite-width neural networks. *arXiv preprint arXiv:2011.14522*, 2020.

TaeHo Yoon, Joo Young Choi, Sehyun Kwon, and Ernest K Ryu. Diffusion probabilistic models generalize when they fail to memorize. In *ICML 2023 Workshop on Structured Probabilistic Inference & Generative Modeling*, 2023.

Huijie Zhang, Jinfan Zhou, Yifu Lu, Minzhe Guo, Peng Wang, Liyue Shen, and Qing Qu. The emergence of reproducibility and generalizability in diffusion models. *arXiv preprint arXiv:2310.05264*, 2023.

A Further Related Work

Theory of diffusion Under mild assumptions on the data distribution, diffusion models achieve a sample complexity scaling exponentially with data dimension (Block et al., 2020; Oko et al., 2023). The sampling and memorization process has been studied for Gaussian mixtures and linear manifolds using the empirical score function (Biroli et al., 2024; Ambrogioni, 2023; Achilli et al., 2024; 2025; Li & Chen, 2024). Learning the empirical score function was studied in (Cui et al., 2023; Shah et al., 2023; Han et al., 2024). The memorization-generalization trade-off in terms of model capacity with random features was studied in George et al. (2025). Generalization bounds for early-stopped random features learning simple score functions were derived in Li et al. (2023). (Biroli & Mézard, 2023; Ambrogioni, 2023; Biroli et al., 2024) show for Gaussian mixtures the existence of a characteristic noise level during the diffusion process where the single modes merge into one. In Biroli et al. (2024), another noise scale is identified, corresponding to short diffusion times, where the backward process collapses into the single training data points, associated with memorization. Kamb & Ganguli (2024) studies generalization in vision diffusion models through the inductive bias of translational equivariance and locality.

Diffusion models for hierarchical data For hierarchically structured data, Sclocchi et al. (2024b;a) show that the reconstruction of high-level features undergoes a phase transition in the diffusion process, while low-level features vary smoothly around the same noise scale. For the same data model, Favero et al. (2025) shows that U-Net diffusion models learn to generate these data by sequentially learning different levels of the grammatical rules, with a sample complexity polynomial in data dimension. Sclocchi et al. (2024b) shows that the Bayes-optimal denoising algorithm for hierarchical data corresponds to belief propagation; Mei (2024) shows that U-Net architectures are able to efficiently approximate this algorithm. Moreover, Garnier-Brun et al. (2024) shows that transformers can implement the same algorithm.

B Experimental Details

B.1 Vision diffusion models

iDDPM In our experiments, we utilize Improved Denoising Diffusion Probabilistic Models (iDDPMs) for image generation on the CIFAR-10 and CelebA datasets, following the codebase of Improved DDPMs (Nichol & Dhariwal, 2021): `https://github.com/openai/improved-diffusion`. Specifically, we train iDDPMs with 256 and 128 channels for CIFAR-10 and CelebA, respectively. Our models are implemented using a U-Net architecture with attention layers and 3 resolution blocks. We use $4,000$ diffusion steps, a cosine noise schedule, a learning rate of 10^{-4}, and a batch size of 128. Training is performed for 262,144 steps using a *hybrid objective* (Nichol & Dhariwal, 2021) and the Adam optimizer with dropout of 0.3.

Stable Diffusion We fine-tune Stable Diffusion v2.1[2] using the codebase `https://github.com/somepago/DCR` from Somepalli et al. (2022; 2023). The model is pre-trained on LAION-2B (Schuhmann et al., 2022) and consists of a latent diffusion U-Net architecture with frozen text and autoencoder components. We fine-tune the U-Net for 262,144 steps on 8,192 images from the LAION-10k dataset at resolution 256×256, using a batch size of 16. We employ a constant learning rate of 5×10^{-6} with 5,000 warm-up steps and use a single image-caption pair per datapoint.

B.2 Language diffusion models

MD4 Our experiments leverage the codebase of MD4 (Shi et al., 2024), available at `https://github.com/google-deepmind/md4`. MD4 is a masked diffusion model that progressively transforms tokens into a special [MASK] token as training proceeds. Specifically, at each timestep t, each non-masked token has a probability β_t of being replaced by [MASK]. The forward transition process for this model can be formally described using a one-hot encoding of the $|\mathcal{V}| + 1$ states, where the transition matrix is defined as:

$$Q_t = (1 - \beta_t)\mathbb{I} + \beta_t \mathbf{1}\mathbf{e}_M^\top. \tag{8}$$

[2] `https://huggingface.co/stabilityai/stable-diffusion-2-1`

Here $\mathbb{I}$ the identity matrix, $\mathbf{1}$ a vector of ones and $\mathbf{e}_M$ the one-hot-encoding vector corresponding to the [MASK] symbol. The entries $[Q_t]_{ij}$ of Q_t indicate the probability of the token x_k transitioning from state i to state j, i.e., $[Q_t]_{ij} = q(x_{k,t} = j | x_{k,t-1} = i)$. At the final timestep T, all tokens are fully masked, i.e., $x_{k,T} = \text{[MASK]}$ for every $k \in [\dim(x)]$. For our experiments, we train MD4 using a batch size of 64 and a context size of 256. All other hyperparameters are kept consistent with the original MD4 implementation.

B.3 Random Hierarchy Model

D3PM For our experiments on the Random Hierarchy Model, we employ convolutional U-Net-based Discrete Denoising Diffusion Probabilistic Models (D3PMs) (Austin et al., 2021). These models are tasked to predict the conditional expectation $\mathbb{E}(x_0|x_t)$, which parameterizes the reverse diffusion process. In particular, we consider a uniform diffusion process (Hoogeboom et al., 2021; Austin et al., 2021), where, at each timestep t, tokens can either stay unchanged or, with probability β_t, can transition to some other symbol in the vocabulary. One-hot encoding the $|\mathcal{V}|$ states, the forward transition matrix formally reads:

$$Q_t = (1 - \beta_t)\mathbb{I} + \frac{\beta_t}{|\mathcal{V}|}\mathbf{1}\mathbf{1}^\top. \tag{9}$$

Here $\mathbb{I}$ is the identity and $\mathbf{1}$ is a vector of all ones. At the final time T, the stationary distribution is uniform over the vocabulary. The convolutional U-Net has L resolution blocks in both the encoder and decoder parts. Each block features the following specification: filter size s, stride s, 8,192 channels per layer, GeLU nonlinearity, skip connections linking encoder and decoder blocks of matching resolution to preserve multi-scale feature information. We include embedding and unembedding layers implemented as convolutional layers with a filter size of 1. This architecture is specifically aligned with the RHM's hierarchical structure, where the filter size and stride of s in the convolutional layers mirror the branching factor of the RHM tree. While this design provides practical benefits in terms of training efficiency, it should not alter the fundamental sample complexity of the problem, as long as the network is sufficiently deep and expressive (Cagnetta et al., 2024). The networks are initialized with the maximal-update (μP) parameterization (Yang & Hu, 2020), ensuring stable feature learning even in the large-width regime. We train with Adam with a learning rate of 0.1 and a batch size of 32. For the diffusion process, we adopt a linear schedule with 1,000 noise levels.

B.4 Hardware

All experiments are run on a single NVIDIA H100 SXM5 GPU with 94GB of RAM.

C Experiments on Stable Diffusion

We consider Stable Diffusion v2.1 (Rombach et al., 2022), a text-to-image latent diffusion model pre-trained on the LAION-2B dataset (Schuhmann et al., 2022). We fine-tune this model for 262,144 steps on $8,192$ samples from the LAION-10k dataset (Somepalli et al., 2023), using a resolution of 256×256. During fine-tuning, the text encoder and encoder-decoder components are kept frozen. We use a held-out validation set of 1,024 image-text pairs to monitor the validation loss. Full training details are provided in Appendix B.

To quantify memorization, we follow the protocol of Somepalli et al. (2022) and compute a similarity score for each generated image based on the cosine similarity of SSCD (Self-Supervised Descriptor for Image Copy Detection) (Pizzi et al., 2022) features, extracted from a ResNet-50 model. Each score is defined as the similarity between a generated image and its nearest neighbor in the training set.

Figure 7(a) plots the training and validation losses as a function of the training step τ. As observed in the main text, initially, both losses decrease, indicating generalization: the model output aligns increasingly with the population score. At a critical time $\tau_{\text{mem}} \propto P$, the validation loss diverges from the training loss, marking the onset of memorization. Early stopping at this point can prevent the model from entering the memorization phase.

In Figure 7(b), we report the similarity scores for 200 generated images at two checkpoints: early stopping ($\tau = 8{,}192$) and the final training step ($\tau = 262{,}144$). For reference, we also show the similarity score for

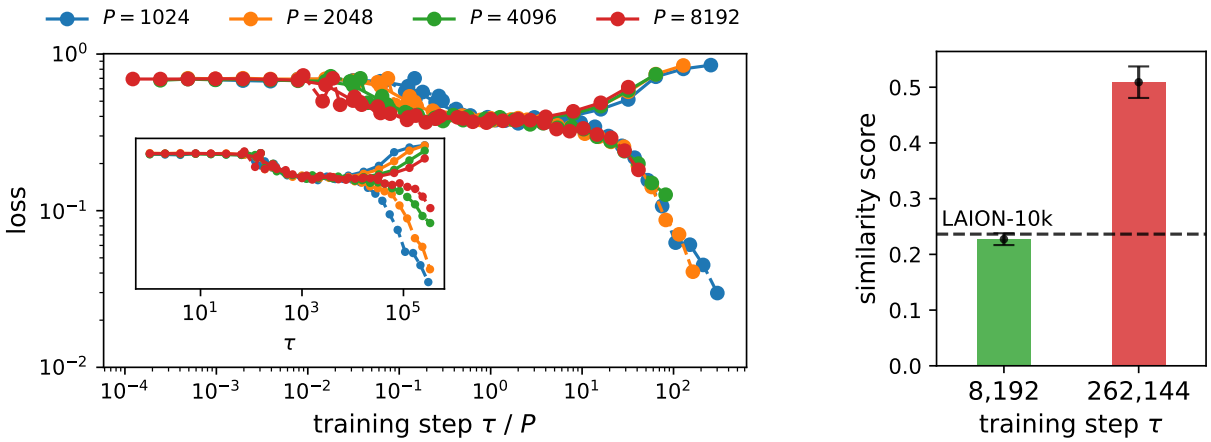

(a) Generalization-memorization dynamics.

(b) Similarity scores.

Figure 7: **Memorization dynamics in Stable Diffusion.** (a) Training and validation losses as a function of training step τ for Stable Diffusion fine-tuned on different subsets of LAION-10k with P training points. Both losses initially decrease, indicating generalization, and diverge at the memorization onset time τ_{mem}. The memorization time τ_{mem} is linear in the training set size P. (b) Cosine similarity scores between SSCD ResNet embedding for generated images and their nearest training neighbor at early stopping ($\tau = 8{,}192$) and final training ($\tau = 262{,}144$). The dashed line indicates the mean similarity score between the closest LAION-10k samples. The sharp increase at late training signals memorization.

Figure 8: **Replicates generated by Stable Diffusion.** Example generations (left) from the final training checkpoint ($\tau = 262{,}144$) with similarity score > 0.5 to their nearest neighbor in the training set (right), confirming memorization.

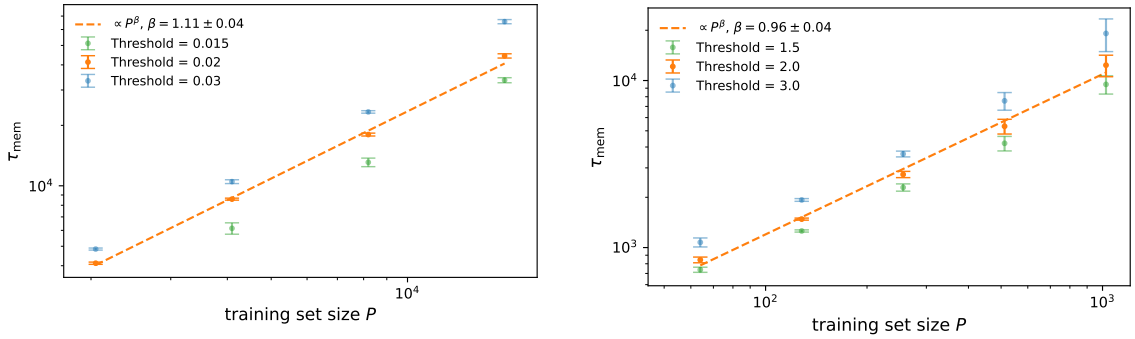

(a) iDDPM on CIFAR-10.

(b) MD4 on text8.

Figure 9: **Scaling of memorization time with dataset size.** For each dataset size P, we linearly interpolate the train and validation losses as a function of the training step τ (on a logarithmic grid) and define the memorization time τ_{mem} as the first step at which the interpolated loss gap $L_{\text{val}}(\tau) - L_{\text{train}}(\tau)$ exceeds a fixed threshold (different colors). We then plot τ_{mem} as a function of P for (a) iDDPMs trained on CIFAR-10 and (b) MD4 language diffusion models trained on text8. In both cases, the data are well described by a power-law fit $\tau_{\text{mem}} \propto P^\beta$ (dashed lines) with exponents β close to one, indicating an approximately linear growth of memorization time with dataset size across modalities. Error bars indicate the sample standard deviation across three independent runs.

real images from the full LAION-10k dataset (black dashed line). At the early stopping time, the generated images exhibit diversity similar to that of the dataset. In contrast, by the end of training, the similarity score increases by a factor of two, indicating memorization.

Finally, in Figure 8, we show representative examples of replicated samples (similarity score > 0.5) from the final checkpoint, confirming that Stable Diffusion memorized part of its training set.

D Further Results on iDDPMs

Scaling of memorization time To further quantify how memorization time scales with dataset size, we estimate a memorization onset time $\tau_{\text{mem}}(P)$ for each number of training examples P. For every setting of P, we record the training and validation losses as a function of the training step τ and linearly interpolate them in τ on a logarithmic grid to obtain dense loss curves. We then consider the difference between validation and training loss and define $\tau_{\text{mem}}(P)$ as the first training time at which this loss gap exceeds a fixed threshold value. The resulting τ_{mem} values for iDDPMs on CIFAR-10 are shown in 9(a), where they are well described by a power-law fit $\tau_{\text{mem}} \propto P^\beta$ with $\beta \approx 1$, indicating an approximately linear growth of memorization time with dataset size.

Extrapolation of memorization time The linear scaling $\tau_{\text{mem}} \propto P$ enables a concrete form of hyper-parameter transfer: τ_{mem} can be calibrated on small training sets and the early-stopping time at larger P extrapolated from the fit. To illustrate this, we fit the power-law $\tau_{\text{mem}} \propto P^\beta$ on iDDPM/CIFAR-10 using only the points with $P \leq 2{,}048$, and use it to predict τ_{mem} at $P = 16{,}384$ – a regime extrapolated to from data calibrated on training sets eight times smaller. The predicted value lies within a relative error of 0.12 of the directly measured τ_{mem}.

Further examples of generations Figure 10 presents further images sampled from the early stopped iDDPM trained on 16,384 CIFAR-10 images.

Examples of copies Figure 11 shows examples of generated samples (top row) and their nearest neighbors in the training set (bottom row) for the iDDPM trained on 8,192 CIFAR-10 images. These examples are

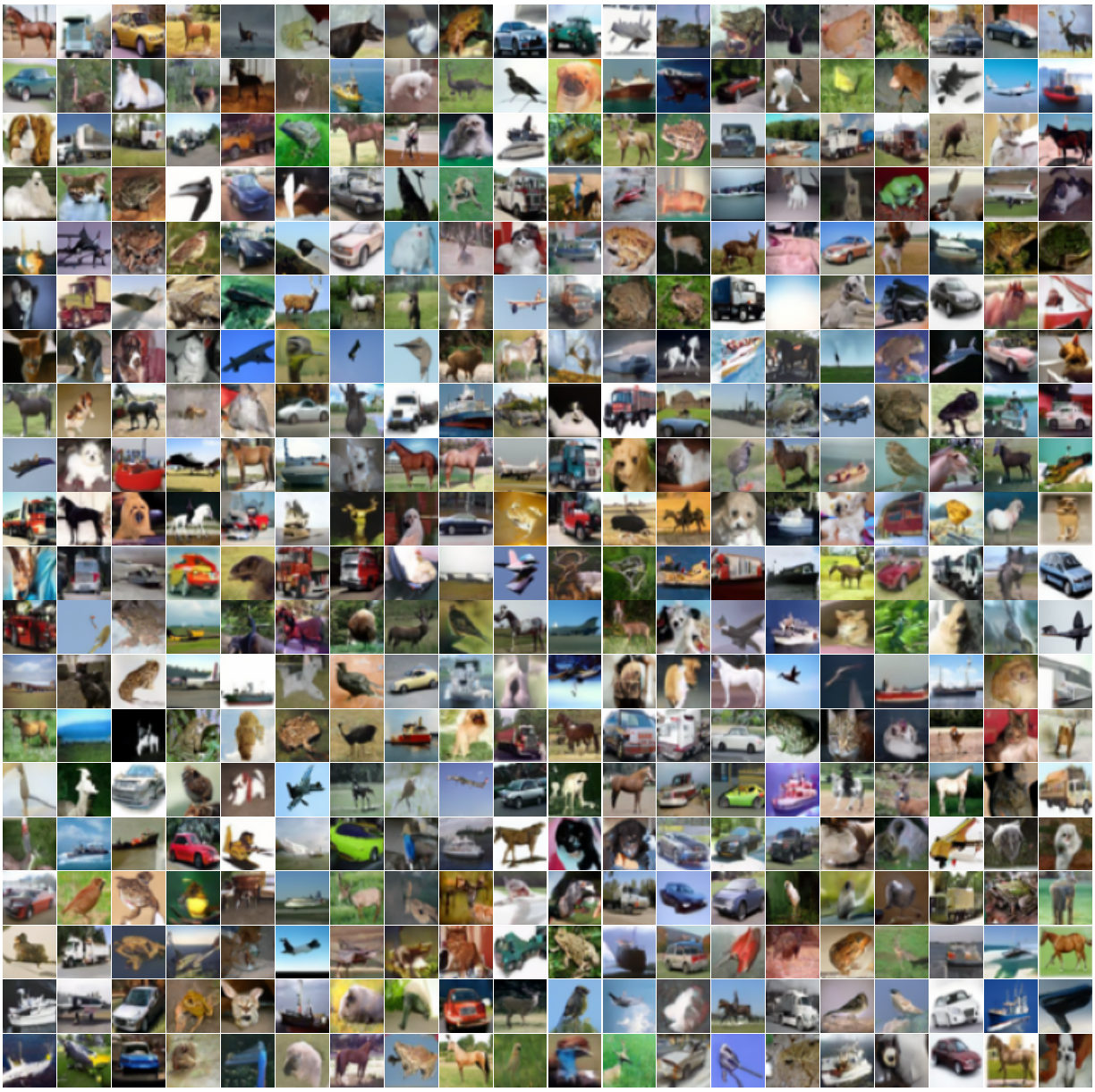

Figure 10: **CIFAR-10 samples generated with early-stopped model.** Additional samples from the iDDPM trained on 16,384 CIFAR-10 images, generated at the early stopping point before memorization. The model produces diverse and high-quality images without replicating the training data.

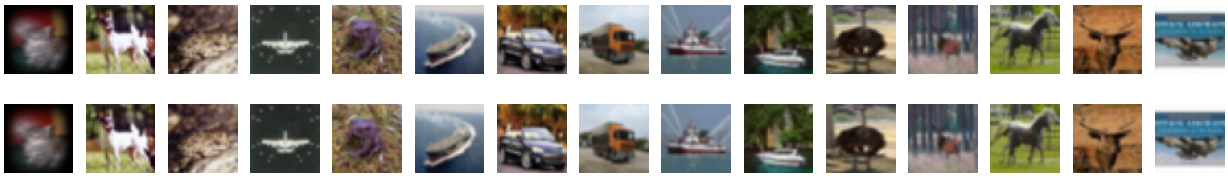

Figure 11: **Examples of copies on CIFAR-10.** Top: samples generated by the iDDPM trained on 8,192 CIFAR-10 images at the end of training. Bottom: nearest neighbors from the training set. The model reproduces specific training examples, indicating memorization.

Generated sample 1

on french anarchism reemerged influencing the bourses de travails af autonomous workers groups and trade unions from this movement the conf d ration g n rale du travail general confederation of work cgt was formed in one eight nine flve as the first major

→

Nearest training sequence

on french anarchism reemerged influencing the bourses de travails of autonomous workers groups and trade unions from this movement the conf d ration g n rale du travail general confederation of work cgt was formed in one eight nine five as the first major

Generated sample 2

erpetual covenant of wareagayndt every people tribe and state ocning a foot of land between here and tierra dul fuego beeause opposition to slavery expansion was the key issue uniting the redublican patty at the time lincol is sometimes critic zed for put

→

Nearest training sequence

erpetual covenant of war against every people tribe and state owning a foot of land between here and tierra del fuego because opposition to slavery expansion was the key issue uniting the republican party at the time lincoln is sometimes criticized for put

Generated sample 3

s with a hagh levul tf intellectual function ne have aspirger s autasm or taat both lypes are merely g eks with a medical label attacied also ausicm has evolved in the public understantingpbot the populariidentification of autism with relatinely severe cas

→

Nearest training sequence

s with a high level of intellectual functioning have asperger s autism or that both types are merely geeks with a medical label attached also autism has evolved in the public understanding but the popular identification of autism with relatively severe cas

Figure 12: **Examples of copies on text8.** Left: Diffusion-generated text with MD4 trained on $1,024$ training sequences of the text8 dataset for $524,288$ SGD steps. Right: the corresponding nearest training sequences. The generated samples are copies of the training set, up to a few character-level mistakes.

taken from the end of training, within the memorization phase, where the model begins to replicate its training data.

E Further Results on MD4

Scaling of memorization time Similarly to DDPMs, in Figure 9(b) we study how the memorization time scales with the number of training examples P for GPT-based MD4 models trained on text8. The resulting τ_{mem} values exhibit a clear power-law dependence on P, $\tau_{\text{mem}} \propto P^{\beta}$, with an exponent β close to one, mirroring the behavior observed for iDDPMs and indicating a similar linear growth of memorization time with dataset size in the language setting.

Examples of copies Figure 12 shows examples of generated samples and their nearest neighbors in the training set for the MD4 trained on 1,024 text8 sequences. These examples are taken from the end of training, within the memorization phase, where the model begins to replicate its training data. In particular, the generated samples are copies of the training set, up to a few character-level mistakes.

F Further Results on the RHM

Production rules sampling Figure 13 shows the mean occurrence and centered covariance of the production rules sampled by a diffusion model trained on $P = 16{,}384$ strings ($v = 16$, $m = 4$, $L = 3$, $s = 2$). The model, trained with early stopping ($\tau = 32{,}768$), samples all RHM rules with a mean occurrence that is ap-

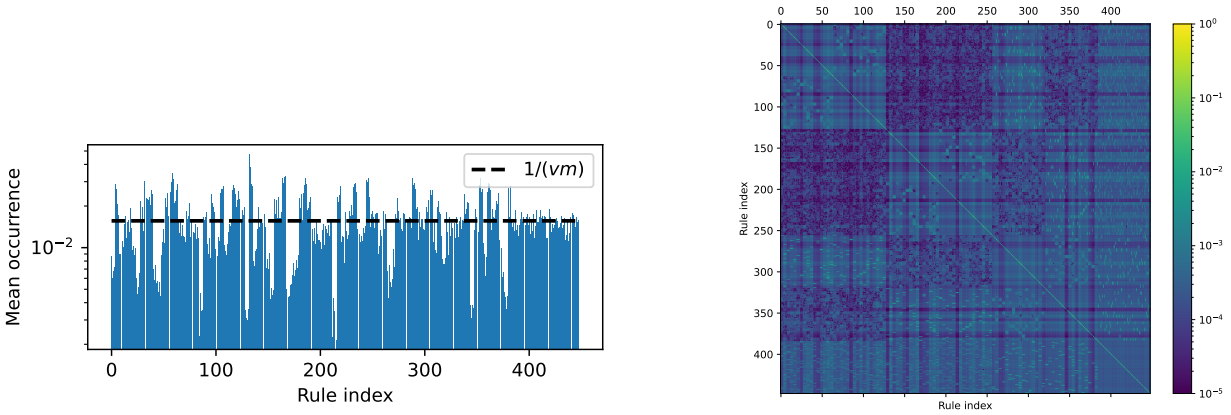

Figure 13: **Sampling of RHM production rules.** Mean occurrence (*left*) and centered covariance (*right*) of the production rules sampled by a diffusion model trained on $P = 16{,}384$ strings ($v = 16$, $m = 4$, $L = 3$, $s = 2$). The model, trained with early stopping ($\tau = 32{,}768$), samples all RHM rules with a mean occurrence that is approximately uniform (up to sampling noise). Likewise, the correlations between the cooccurrence of sampled rules show that they are sampled approximately independently.

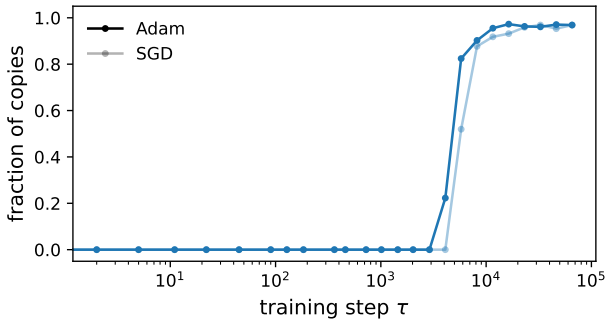

Figure 14: **Effect of the optimizer on the onset of memorization in the RHM.** Fraction of copies as a function of training step for a D3PM trained on $P = 2,048$ sequences sampled from an RHM with $L = 3$, $s = 3$, $v = 24$, $m = 12$, using Adam and SGD, each with its maximal stable learning rate (largest learning rate yielding convergent training loss). The curves nearly coincide, and the onset of memorization occurs at approximately the same number of training steps for both optimizers.

proximately uniform (up to sampling noise); likewise, the correlations between the cooccurrence of sampled rules show that they are sampled approximately independently. Therefore, the generated data reproduces the correct data distribution of the RHM, corresponding to generalization.

Robustness to optimizer choice To test robustness to the optimization dynamics, we repeated the RHM experiments with $L = 3$, $s = 3$, $v = 24$, $m = 12$ using the same D3PM architecture and training protocol as in the main text, varying only the optimizer between Adam and SGD. For each optimizer, we set the learning rate to its *maximal stable* learning rate, defined as the largest value for which the training loss reliably converges. Figure 14 confirms the robustness of τ_{mem} to the choice of optimizer in this setting.

G Scaling argument for the memorization time of kernel methods

In this appendix, we present a scaling argument in a tractable kernel regime for learning the empirical score at a fixed low diffusion noise level σ. In particular, our goal is to identify the timescale associated with fitting the empirical score.

The logic is the following. First, under kernel gradient flow, spectral modes of the kernel operator are learned at rates given by their eigenvalues. Second, in the low-noise regime, the empirical score near a training point is a localized odd linear field. Third, we probe the kernel operator along localized odd test functions matching this local structure. Their Rayleigh quotient provides a variational estimate of the relevant local spectral scale, and a lower bound on the slowest eigen-timescale present in that direction.

For simplicity, we work with one scalar component of the score. The vector-valued statement follows coordinate-wise.

Setting Let $x_1, \dots, x_P \in \mathbb{R}^d$ be P distinct training points, and consider the Gaussian-smoothed empirical distribution

$$p_\sigma(x) = \frac{1}{P}\sum_{j=1}^{P} \mu_j(x), \qquad \mu_j(x) := \mathcal{N}(x \mid x_j, \sigma^2 I_d). \tag{10}$$

Its score is

$$g_\sigma(x) := \nabla_x \log p_\sigma(x). \tag{11}$$

We consider a scalar kernel method with an isotropic kernel

$$K(x, y) = \kappa(\|x - y\|), \tag{12}$$

and assume that κ has the local expansion

$$\kappa(r) = \kappa(0) - C_K r^\nu + O(r^{\nu+\eta}) \qquad (r \to 0), \tag{13}$$

for some constants $C_K > 0$, $\nu > 0$, and $\eta > 0$. For instance, for data normalized on the unit hypersphere, $\nu = 1$ for the ReLU NTK, while $\nu = 2$ for random-feature kernels.

Let T_K be the kernel integral operator on $L_2(p_\sigma)$,

$$(T_K f)(x) = \int K(x, y) f(y)\, dp_\sigma(y). \tag{14}$$

Kernel gradient flow and mode-wise learning times We now recall the standard connection between kernel gradient flow and spectral learning times.

Let $h_\sigma \in L_2(p_\sigma)$ be a target scalar function to be learned at the fixed noise level σ. In our application, h_σ will be one component of the score g_σ. We consider the kernel gradient-flow dynamics

$$\partial_\tau f_\tau = T_K\big(h_\sigma - f_\tau\big), \qquad f_{\tau=0} = 0. \tag{15}$$

Equivalently, the error $e_\tau := h_\sigma - f_\tau$ satisfies

$$\partial_\tau e_\tau = -T_K e_\tau, \qquad e_{\tau=0} = h_\sigma. \tag{16}$$

Let $(\lambda_m, \varphi_m)_{m\geq 1}$ be an orthonormal eigenbasis of T_K in $L_2(p_\sigma)$, so that

$$T_K \varphi_m = \lambda_m \varphi_m, \qquad \lambda_m \geq 0. \tag{17}$$

Then the error evolves as

$$e_\tau = \sum_{m\geq 1} e^{-\lambda_m \tau} \langle h_\sigma, \varphi_m \rangle_{L_2(p_\sigma)}\, \varphi_m. \tag{18}$$

In particular,

$$\langle e_\tau, \varphi_m \rangle_{L_2(p_\sigma)} = e^{-\lambda_m \tau} \langle h_\sigma, \varphi_m \rangle_{L_2(p_\sigma)}. \tag{19}$$

Therefore, a spectral mode with eigenvalue λ_m is learned on a timescale proportional to $1/\lambda_m$.

Proof. Since T_K is self-adjoint and positive on $L_2(p_\sigma)$, we may expand the initial error $e_0 = h_\sigma$ in its eigenbasis:

$$h_\sigma = \sum_{m\geq 1} \langle h_\sigma, \varphi_m\rangle_{L_2(p_\sigma)}\, \varphi_m. \tag{20}$$

Equation 16 then decouples mode by mode:

$$\partial_\tau \langle e_\tau, \varphi_m\rangle_{L_2(p_\sigma)} = -\lambda_m \langle e_\tau, \varphi_m\rangle_{L_2(p_\sigma)}. \tag{21}$$

Solving this ODE yields equation 19, hence equation 18. □

Thus, to understand the learning time of the *memorization part* of the target, one has to identify the relevant spectral scale of the kernel operator on the corresponding directions.

G.1 Scorelets and memorization

Let $\Delta := \min_{i\neq j} \|x_i - x_j\|$ be the minimum distance between training points, and assume the low-noise separated regime

$$\sigma \ll \Delta. \tag{22}$$

Fix a training point x_i, and consider x such that $\|x - x_i\| = O(\sigma)$. Then the i-th Gaussian component dominates the mixture equation 10, and the score is locally

$$g_\sigma(x) = -\frac{x - x_i}{\sigma^2} + O\Big(e^{-c/\sigma^2}\Big), \tag{23}$$

for some constant $c > 0$ depending on the point configuration. More precisely, the correction comes from the exponentially small overlap with the other Gaussian components.

Equation 23 shows that, near each training point, the empirical score is:

- localized on a ball of radius $O(\sigma)$,
- odd with respect to the center x_i,
- linear to leading order.

This is the point-specific local structure that must be learned in order to memorize the empirical distribution.

We therefore introduce, for every $i \in [P]$ and every unit vector $u \in \mathbb{S}^{d-1}$, the *scorelet*

$$\phi_{i,u}(x) = u^\top (x - x_i)\, R\Big(\frac{\|x - x_i\|}{\sigma}\Big), \tag{24}$$

where $R : [0, \infty) \to \mathbb{R}$ is a fixed smooth radial cutoff, compactly supported and not identically zero. The scorelets have the same qualitative structure as the local score field: they are localized, odd, and linear near x_i. The index i selects the training point, while the direction u selects one local coordinate of the score.

To see that these directions are genuinely present in the target, define the scalar score component

$$h_{\sigma,u}(x) := u^\top g_\sigma(x). \tag{25}$$

Then, using equation 23, one finds

$$\langle h_{\sigma,u}, \phi_{i,u}\rangle_{L_2(p_\sigma)} = -\frac{\widetilde{\gamma}_{d,R}}{P} + O\Big(e^{-c/\sigma^2}\Big), \tag{26}$$

where

$$\widetilde{\gamma}_{d,R} := \int z_1^2 R(\|z\|)\, \varphi_d(z)\, dz > 0, \qquad \varphi_d(z) := (2\pi)^{-d/2} e^{-\|z\|^2/2}. \tag{27}$$

Hence the target has nonzero overlap with each scorelet $\phi_{i,u}$. This is why these are the natural directions to study when analyzing memorization.

G.2 Rayleigh quotient

We now compute the scale of the kernel operator on the localized probes.

For a fixed i and u, define the Rayleigh quotient

$$\mathcal{R}_{i,u}(\sigma, P) := \frac{\langle \phi_{i,u}, T_K \phi_{i,u} \rangle_{L_2(p_\sigma)}}{\|\phi_{i,u}\|^2_{L_2(p_\sigma)}}. \tag{28}$$

Writing the scorelet in the eigenbasis of T_K as

$$\phi_{i,u} = \sum_{m \geq 1} a_m \varphi_m, \tag{29}$$

one has

$$\mathcal{R}_{i,u}(\sigma, P) = \frac{\sum_{m \geq 1} \lambda_m |a_m|^2}{\sum_{m \geq 1} |a_m|^2}. \tag{30}$$

Hence $\mathcal{R}_{i,u}$ is the weighted average of the eigenvalues excited by the scorelet. In particular, if

$$\lambda^{\text{exc}}_{\min}(i, u) := \min\{\lambda_m : \ a_m \neq 0\}, \tag{31}$$

then

$$\lambda^{\text{exc}}_{\min}(i, u) \leq \mathcal{R}_{i,u}(\sigma, P), \qquad \text{so} \qquad \mathcal{R}_{i,u}(\sigma, P)^{-1} \leq \left(\lambda^{\text{exc}}_{\min}(i, u)\right)^{-1}. \tag{32}$$

Therefore, the inverse Rayleigh quotient lower-bounds the slowest eigen-timescale present in the localized direction $\phi_{i,u}$.

To state the main result, introduce the constants

$$\gamma_{d,R} := \int z_1^2 R(\|z\|)^2 \varphi_d(z)\, dz, \tag{33}$$

and

$$\beta_{d,\nu,R} := -\iint z_1 w_1 R(\|z\|) R(\|w\|) \|z - w\|^\nu \varphi_d(z) \varphi_d(w)\, dz\, dw. \tag{34}$$

By rotational symmetry, these definitions do not depend on the choice of coordinate z_1. We assume that R has been chosen so that

$$\gamma_{d,R} > 0, \qquad \beta_{d,\nu,R} > 0. \tag{35}$$

Proposition 2. *Fix a configuration of pairwise distinct training points $x_1, \ldots, x_P$, and assume the low-noise separated regime $\sigma \ll \Delta$. Then, for every $i \in [P]$ and every unit vector $u \in \mathbb{S}^{d-1}$,*

$$\|\phi_{i,u}\|^2_{L_2(p_\sigma)} = \frac{\sigma^2}{P} \gamma_{d,R} + O\left(e^{-c/\sigma^2}\right), \tag{36}$$

and

$$\langle \phi_{i,u}, T_K \phi_{i,u} \rangle_{L_2(p_\sigma)} = C_K\, \beta_{d,\nu,R} \frac{\sigma^{2+\nu}}{P^2} + O\left(\frac{\sigma^{2+\nu+\eta}}{P^2}\right) + O\left(e^{-c/\sigma^2}\right), \tag{37}$$

for some constant $c > 0$ depending on the point configuration. Consequently,

$$\mathcal{R}_{i,u}(\sigma, P) = \frac{C_K\, \beta_{d,\nu,R}}{\gamma_{d,R}} \frac{\sigma^\nu}{P} + O\left(\frac{\sigma^{\nu+\eta}}{P}\right) + O\left(e^{-c/\sigma^2}\right). \tag{38}$$

In particular, at fixed low noise σ, the leading dependence on the dataset size is exactly P^{-1}.

Proof. We fix $i \in [P]$ and $u \in \mathbb{S}^{d-1}$, and write $\phi = \phi_{i,u}$.

Using $p_\sigma = \frac{1}{P}\sum_{j=1}^{P}\mu_j$,

$$\|\phi\|^2_{L_2(p_\sigma)} = \frac{1}{P}\sum_{j=1}^{P}\int \phi(x)^2\mu_j(x)\,dx. \tag{39}$$

The contribution of $j = i$ is obtained by the change of variables $x = x_i + \sigma z$:

$$\frac{1}{P}\int \phi(x)^2\mu_i(x)\,dx = \frac{1}{P}\int \big(u^\top(x - x_i)\big)^2 R\Big(\frac{\|x - x_i\|}{\sigma}\Big)^2 \mu_i(x)\,dx \tag{40}$$

$$= \frac{\sigma^2}{P}\int (u^\top z)^2 R(\|z\|)^2\varphi_d(z)\,dz = \frac{\sigma^2}{P}\,\gamma_{d,R}. \tag{41}$$

Because ϕ is supported in a ball of radius $O(\sigma)$ around x_i, every term with $j \neq i$ is exponentially small in the separated regime $\sigma \ll \Delta$. Summing them gives the remainder in equation 36.

By definition,

$$\langle \phi, T_K\phi\rangle_{L_2(p_\sigma)} = \iint \phi(x)\phi(y)K(x, y)\,dp_\sigma(x)\,dp_\sigma(y). \tag{42}$$

The dominant contribution comes from the i-th Gaussian component in both variables:

$$\frac{1}{P^2}\iint \phi(x)\phi(y)\kappa(\|x - y\|)\mu_i(x)\mu_i(y)\,dx\,dy. \tag{43}$$

Since ϕ is odd around x_i whereas μ_i is even around x_i,

$$\int \phi(x)\mu_i(x)\,dx = 0. \tag{44}$$

Therefore the constant term $\kappa(0)$ in equation 13 does not contribute to equation 43. Only the first nonconstant term matters. Substituting the expansion equation 13 gives

$$\begin{aligned}\text{equation 43} = &-\frac{C_K}{P^2}\iint \phi(x)\phi(y)\|x - y\|^\nu\mu_i(x)\mu_i(y)\,dx\,dy \\ &+ O\Big(\frac{1}{P^2}\iint |\phi(x)\phi(y)|\,\|x - y\|^{\nu+\eta}\mu_i(x)\mu_i(y)\,dx\,dy\Big).\end{aligned} \tag{45}$$

We now change variables $x = x_i + \sigma z$, $y = x_i + \sigma w$. Using

$$\phi(x) = \sigma\, u^\top z\, R(\|z\|), \qquad \|x - y\| = \sigma\|z - w\|, \tag{46}$$

we obtain

$$\text{equation 43} = C_K\,\beta_{d,\nu,R}\,\frac{\sigma^{2+\nu}}{P^2} + O\Big(\frac{\sigma^{2+\nu+\eta}}{P^2}\Big). \tag{47}$$

Notice that all terms involving at least one Gaussian component μ_j with $j \neq i$ are exponentially small in the separated regime, because ϕ is supported in an $O(\sigma)$-ball around x_i. They contribute the remainder $O(e^{-c/\sigma^2})$ in equation 37.

Combining equation 36 and equation 37 yields

$$\mathcal{R}_{i,u}(\sigma, P) = \frac{C_K\,\beta_{d,\nu,R}}{\gamma_{d,R}}\,\frac{\sigma^\nu}{P} + O\Big(\frac{\sigma^{\nu+\eta}}{P}\Big) + O\Big(e^{-c/\sigma^2}\Big), \tag{48}$$

which is equation 38. □

G.3 Localized spectral timescale

As discussed above, an exact eigenmode with eigenvalue λ is learned on a timescale proportional to $1/\lambda$. Proposition 2 shows that the localized sample-specific directions $\phi_{i,u}$ sit at spectral scale

$$\mathcal{R}_{i,u}(\sigma, P) = C_{\text{loc}} \frac{\sigma^{\nu}}{P} + O\left(\frac{\sigma^{\nu+\eta}}{P}\right) + O\left(e^{-c/\sigma^2}\right), \qquad C_{\text{loc}} := \frac{C_K\, \beta_{d,\nu,R}}{\gamma_{d,R}}. \tag{49}$$

This motivates the definition of the *localized spectral timescale*

$$\tau_{\text{loc}}^{(i,u)} := \mathcal{R}_{i,u}(\sigma, P)^{-1}. \tag{50}$$

Hence, at fixed low noise, the leading dependence is

$$\tau_{\text{loc}}^{(i,u)} \propto \frac{P}{\sigma^{\nu}}. \tag{51}$$

The quantity $\tau_{\text{loc}}^{(i,u)}$ is a lower bound on the slowest eigen-timescale present in that localized direction, and more generally a variational proxy for the corresponding learning time. This suggests a memorization time proportional to P at fixed low noise.

All in all, this argument extends the results from contemporaneous work on random features in the proportional regime (number of neurons proportional to the input dimension) (Bonnaire et al., 2025) to any isotropic kernels. Our derivation relies only on the local behavior of the kernel and shows that random features and neural networks in the NTK limit have different behavior with respect to diffusion noise.

G.4 Numerical experiments

We confirm our theoretical prediction numerically in Figure 15 for a one-hidden-layer fully-connected network in the lazy (NTK) regime (Chizat et al., 2019). Notably, the same experimental setting under a mean-field (feature learning) initialization (Mei et al., 2018) also exhibits a memorization time consistent with our NTK-based prediction.

Furthermore, Figure 17 investigates the effect of batch size B. For both lazy and feature learning regimes, the timescale to fit the empirical score appears independent of B, from small-batch SGD ($B = 8$) to full-batch gradient descent ($B = P$). This observation implies that the memorization time only depends on the size of the training set and not on the number of times a training point is observed.

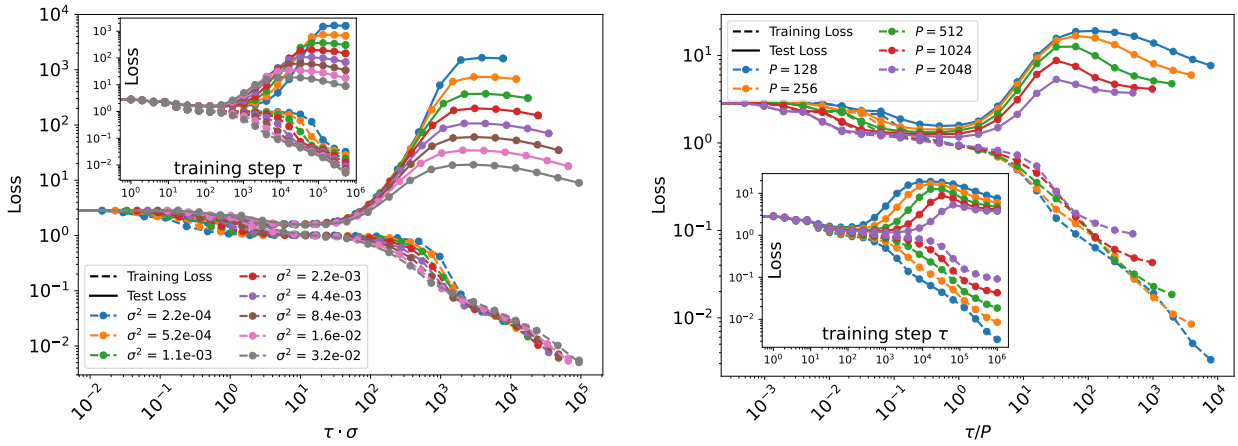

Figure 15: **Neural Tangent Kernel (NTK) initialization: one-hidden layer ReLU neural network (width 8192) learning the empirical score at fixed diffusion noise variance σ^2, trained with full-batch gradient descent.** Training points sampled from a Gaussian distribution in $d = 64$ dimensions. *Left*: at fixed training set size $P = 128$, training and test loss diverge at a timescale (τ_{mem}) depending on σ (inset), which scales as σ^{-1} (main). *Right*: at fixed $\sigma^2 = 3.2 \cdot 10^{-2}$, τ_{mem} increases with P (inset), consistently with the scaling $\tau_{\text{mem}} \propto P$ (main).

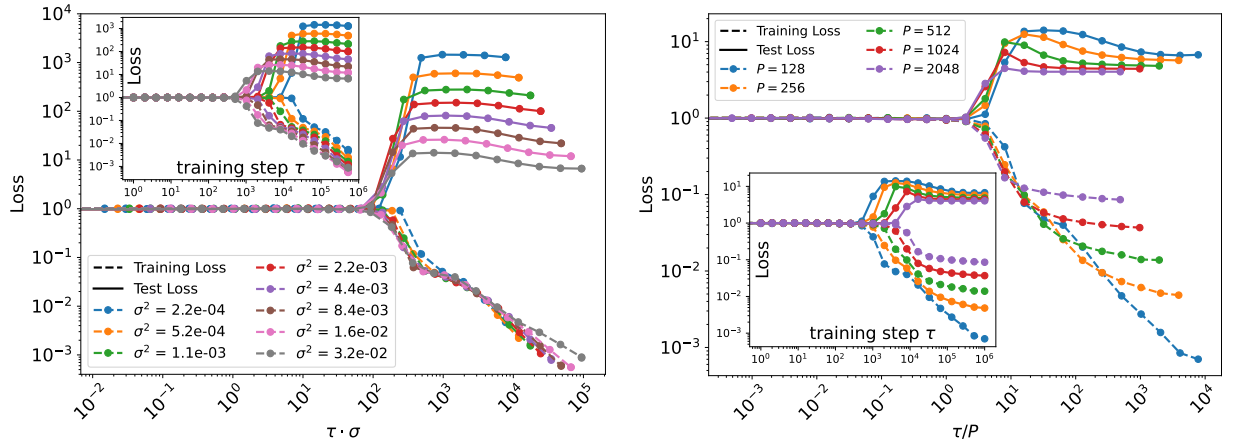

Figure 16: **Feature learning (mean-field) initialization, same setting as Figure 15.** Also in this case, τ_{mem} is compatible with the scaling $\tau_{\text{mem}} \sim \sigma^{-1}$ at fixed P (*left*), and $\tau_{\text{mem}} \propto P$ at fixed σ (*right*).

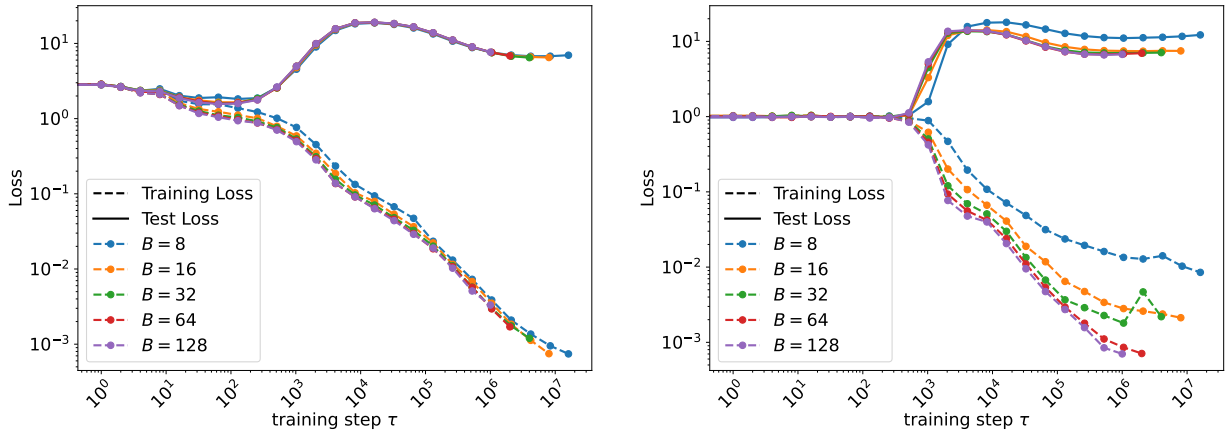

Figure 17: **Effect of changing batch size B, same setting as Figs. 15 and 16** (fixed $\sigma^2 = 3.2 \cdot 10^{-2}$, $P = 128$). Varying the batch size B of training, both with the NTK (*left*) and feature learning (*right*) initialization, does not affect τ_{mem}.

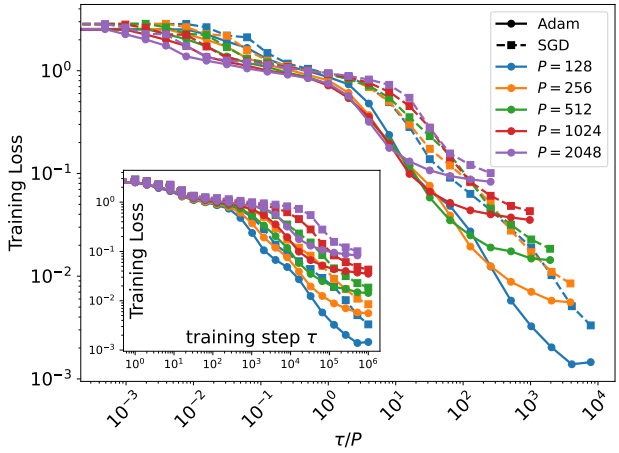

Figure 18: **Optimizer dependence.** Training loss as a function of training step for a one-hidden-layer ReLU neural network (NTK initialization) trained with Adam and SGD at multiple dataset sizes P. For each optimizer, we choose its maximal stable learning rate, defined as the largest learning rate for which the training loss reliably converges. For both optimizers, the curves at different P start decaying at the same point when plotted against τ/P, indicating the same linear scaling of the characteristic training time with P. Adam and SGD differ only by a horizontal shift, corresponding to an $O_P(1)$ change in the constant of proportionality. The overall scaling and decay of the loss remain essentially identical. The inset shows the same data as a function of the unscaled training step τ.